The Astronomical Journal, 171:90 (21pp), 2026 February https://doi.org/10.3847/1538-3881/ae27bd

Predictions of the LSST Solar System Yield: Neptune Trojans

Joseph Murtagh[1], Megan E. Schwamb[1], Pedro H. Bernardinelli[2,3,17], Hsing Wen Lin (林省 文)[4,5], Jacob A. Kurlander[3], Stephanie R. Merritt[1], Samuel Cornwall[6], Mario Jurić[2,3], Grigori Fedorets[7,8], Matthew J. Holman[9], Siegfried Eggl[6,10], R. Lynne Jones[11,12], Peter Yoachim[2,3], Joachim Moeyens[1,3,13], Jeremy Kubica[14,15], Drew Oldag[2,3,15], Maxine West[2,3,15], and Colin Orion Chandler[2,3,15,16]

[1] Astrophysics Research Centre, School of Mathematics and Physics, Queen's University Belfast, Belfast, BT7 1NN, UK; jmurtagh05@qub.ac.uk
[2] DiRAC Institute, University of Washington, 3910 15th Ave NE, Seattle, WA 98195-1560, USA
[3] Department of Astronomy, University of Washington, 3910 15th Ave NE, Seattle, WA 98195-1700, USA
[4] Department of Physics, University of Michigan, Ann Arbor, MI 48109, USA
[5] Michigan Institute for Data and AI in Society, University of Michigan, Ann Arbor, MI 48109, USA
[6] Department of Aerospace Engineering, Grainger College of Engineering, University of Illinois at Urbana-Champaign, Urbana, IL 62802, USA
[7] Finnish Centre for Astronomy with ESO, University of Turku, FI-20014 Turku, Finland
[8] Department of Physics, University of Helsinki, P.O. Box 64, 00014, Finland
[9] Center for Astrophysics | Harvard & Smithsonian, 60 Garden St, Cambridge, MA 02138, USA
[10] Department of Astronomy, University of Illinois at Urbana-Champaign, Urbana, IL 61801, USA
[11] Rubin Observatory, 950 N. Cherry Ave, Tucson, AZ 85719, USA
[12] Aston Carter, Suite 150, 4321 Still Creek Dr, Burnaby, BC V5C 6S7, Canada
[13] Asteroid Institute, 20 Sunnyside Ave, Suite 427, Mill Valley, CA 94941, USA
[14] McWilliams Center for Cosmology, Department of Physics, Carnegie Mellon University, Pittsburgh, PA 15213, USA
[15] LSST Interdisciplinary Network for Collaboration and Computing Frameworks, 933 N. Cherry Ave, Tucson, AZ 85721, USA
[16] Department of Astronomy and Planetary Science, Northern Arizona University, Flagstaff, AZ 86011, USA

Received 2025 September 17; revised 2025 November 24; accepted 2025 November 28; published 2026 January 20

Abstract

The NSF-DOE Vera C. Rubin Observatory's Legacy Survey of Space and Time (LSST), beginning full operations in late 2025, will dramatically transform solar system science by vastly expanding discoveries and providing detailed characterization opportunities across all small-body populations. This includes the co-orbiting 1:1 resonant Neptune Trojans (NTs), which are thought to be dynamically hot captures from the protoplanetary disk. Using the survey simulator `Sorcha`, combined with the latest LSST cadence simulations, we present the very first predictions for the NT yield within the LSST. We forecast a model-dependent median number of ∼130–300 discovered NTs, and infer a notable 2:1 detection bias toward the recently emerged L5 cloud near the Galactic plane versus the L4 cloud, reflecting the lower-cadence coverage in the Northern Ecliptic Spur region that suppresses L4 detections. The additionally simulated Science Validation survey will offer the very first early insights into this understudied cloud. Around 60% of detected main survey NTs will meet stringent color light-curve quality criteria, increasing the sample size more than fourfold compared to existing datasets. This enhanced sample will enable robust statistical analyses of NT color and size distributions, crucial for understanding their origins and relationship to the broader trans-Neptunian population. These comprehensive color measurements represent a major step forward in characterizing the NT population and will facilitate future targeted spectroscopic observations.

Unified Astronomy Thesaurus concepts: Neptune trojans (1097); Neptunian satellites (1098); Trojan asteroids (1715); Small Solar System bodies (1469); Sky surveys (1464)

1. Introduction

The Neptune Trojans (NTs) are a class of minor solar system body which co-orbit with Neptune (semimajor axis $a \sim 30.1$ au), librating around the 1:1 mean-motion resonance with the giant planet. As with other Trojans, the NTs reside in the L4 (leading) and L5 (trailing) Lagrange points of Neptune. The 1:1 resonance (as with Neptune's other n:1 resonances) admits both symmetric (relative to the relative mean longitude $\lambda - \lambda_N$, also known as a horseshoe orbit; C. D. Murray & S. F. Dermott 1999; G. Voyatzis & J. D. Hadjidemetriou 2005) and asymmetric (or tadpole orbit) librators (S. F. Dermott & C. D. Murray 1981; S. J. Peale 1986; C. Beauge 1994; R. Malhotra 1996; R. A. Murray-Clay & E. I. Chiang 2005; B. Gladman et al. 2012; R. E. Pike et al. 2015; K. Volk et al. 2018; Y.-T. Chen et al. 2019). Numerical simulations have shown that some known symmetric librators have dynamical stability on the order of ∼Myr, implying they are only temporary captures from, e.g., the Centaur population (J. Horner & N. W. Evans 2006; J. Horner & P. S. Lykawka 2010, 2012; C. de la Fuente Marcos & R. de la Fuente Marcos 2012; P. Guan et al. 2012; J. Horner et al. 2012; M. Alexandersen et al. 2013; H. W. Lin et al. 2016; R.-j. Wu et al. 2019). On the other hand, the asymmetric librators have been shown to be long-lived on the scale of ∼Gyr, suggesting that these NTs are remnants of the early solar system, captured in Neptune's outwards migration (F. Marzari et al. 2003; R. Brasser et al. 2004; S. J. Kortenkamp et al. 2004; L.-Y. Zhou et al. 2009, 2011; P. S. Lykawka et al. 2011; P. Guan et al. 2012; H. W. Lin et al. 2016, 2021;

---

[17] DiRAC Post-doctoral Fellow.

R.-j. Wu et al. 2019; H.-W. Lin et al. 2022). Recent modeling has shown that the present-day NT clouds may in fact be only a small remnant of this primordial population, with only ∼1% surviving after 4 Gyr (P. S. Lykawka et al. 2009). Most importantly, however, is that these stable NTs (both those captured and those formed in situ; P. S. Lykawka et al. 2009, 2011) are therefore expected to preserve a fossil record of their source region, with their inclination i, eccentricity e, and surface-color distributions remaining largely unaltered over these ∼Gyr timescales (P. S. Lykawka et al. 2009, 2010, 2011; D. Nesvorný & D. Vokrouhlický 2009; P. S. Lykawka & J. Horner 2010; A. H. Parker 2015; Y.-Y. Chen et al. 2016; R. Gomes & D. Nesvorný 2016). As these elements are effectively unchanged since emplacement into the resonance, the present-day orbital and color distributions can be compared quantitatively with capture and migration models of the protoplanetary disk. A well-characterized sample of NTs could therefore assist in discriminating between competing migration scenarios (e.g., D. Nesvorný & A. Morbidelli 2012) and inform the early dynamical evolution of the outer solar system.

The known NT population is, however, relatively small, being composed of discoveries from several surveys (J. L. Elliot et al. 2005; S. S. Sheppard & C. A. Trujillo 2006, 2010a; M. Alexandersen et al. 2013; A. H. Parker et al. 2013; D. W. Gerdes et al. 2016; M. T. Bannister et al. 2018; H. W. Lin et al. 2019; P. H. Bernardinelli et al. 2022). The Minor Planet Center (MPC) only lists 31 NTs at the time of writing,[18] with the vast majority being located within the L4 cloud (27 L4 versus four L5). This asymmetry is almost certainly due to the observational bias of the L5 cloud having resided in the crowded Galactic plane for at least the past two decades, making the discovery of L5 NTs extremely challenging. The first discovery of an L5 NT by S. S. Sheppard & C. A. Trujillo (2010a) implied a symmetrical distribution of L4 and L5 clouds, with numerical simulations from E. I. Chiang & Y. Lithwick (2005) predicting them to be at least as numerous as the Jupiter Trojans. Many of the known L5 NTs have been shown to be dynamically unstable—such as 2013 KY_{18} (H. W. Lin et al. 2016), 2004 KV_{18} (P. Guan et al. 2012; J. Horner & P. S. Lykawka 2012), and 2008 LC_{18} (J. Horner et al. 2012)—suggesting that these objects are temporary captures, and reinforcing the potential for asymmetric cloud sizes. Although relatively few NTs have been detected to date, limiting the precision of population-wide constraints, ongoing studies have begun to characterize their total population sizes, size–frequency distributions, and surface colors. Early color measurements initially suggested that NTs may share similarly bimodal surface-color distributions as with the Jupiter Trojans (S. S. Sheppard & C. A. Trujillo 2006; S. S. Sheppard 2012; A. H. Parker et al. 2013; D. W. Gerdes et al. 2016; D. Jewitt 2018; H. W. Lin et al. 2019; B. T. Bolin et al. 2023), although more recent surveys from L. Markwardt et al. (2023) and B. T. Bolin et al. (2023) show that this may be a result of a lack of observations. Long-term collisional and dynamical models show that impacts between NTs and, e.g., the Plutino population, while relatively rare over Gyr timescales (A. J. C. Almeida et al. 2009), may contribute to additional fragmentation and shared surface colors of both populations (P. Thébault & A. Doressoundiram 2003; G. C. de Elía et al. 2008; A. J. C. Almeida et al. 2009; D. Nesvorný & D. Vokrouhlický 2009; H. W. Lin et al. 2021; L. Markwardt et al. 2025). While NTs are clearly a potentially highly informative population, current observations provide only a small, biased glimpse of their true underlying distribution.

The NSF-DOE Vera C. Rubin Observatory’s Legacy Survey of Space and Time (LSST; LSST Science Collaboration et al. 2009; Ž. Ivezić et al. 2019; F. B. Bianco et al. 2022) will dramatically advance our knowledge of the entire solar system. With its effective 6.5 m aperture and ∼9.6 deg^2 field of view, it will image the entire southern night sky approximately every three nights in six optical *ugrizy* bands, all over a 10 yr observational baseline. The “wide-fast-deep” (WFD) portion of the survey will cover ∼18,000 deg^2 repeatedly (with ∼800 visits per field) to a single-visit depth of $m_r \sim 24.7$ (or ∼27.5 in coadded images; LSST Science Collaboration et al. 2009; Ž. Ivezić et al. 2019; F. B. Bianco et al. 2022). Per R. L. Jones et al. (2020) and SCOC (2024), the LSST will also allocate ∼10% of its observing cadence time to mini-surveys. In particular for solar system science, the largest components include the Deep Drilling Fields (DDFs; six dedicated ∼10 deg^2 survey areas, which will receive a higher cadence of visits to achieve deeper coadd magnitude depths) and the Northern Ecliptic Spur (NES; an extension in *griz* observations of the WFD by +10° ecliptic latitude; M. E. Schwamb et al. 2018, 2023). The combination of its wide field of view, faint sensitivity, multiband imaging, and dense observational cadence make the LSST particularly suited to detecting solar system objects. Prior studies have predicted that the near-Earth objects, main-belt asteroids, Jupiter Trojans, and trans-Neptunian objects (TNOs) will all receive a ∼tenfold increase in their respective populations (R. L. Jones et al. 2009, 2018; LSST Science Collaboration et al. 2009; M. Solontoi et al. 2010; A. Shannon et al. 2015; T. Grav et al. 2016; K. Silsbee & S. Tremaine 2016; P. Vereš & S. R. Chesley 2017; S. Eggl et al. 2019; Ž. Ivezić et al. 2019; G. Fedorets et al. 2020; D. J. Hoover et al. 2022). More recently, J. A. Kurlander et al. (2025) more precisely predict a ∼fourfold to tenfold for these populations, with J. Murtagh et al. (2025) predicting a ∼sevenfold increase for the Centaurs. It is logical to expect that the LSST will therefore also be capable of vastly increasing the known NT sample size as it not only probes down to depths of $m_r \sim 24.7$, but also tiles more of the entire southern night sky across multiple filters than previous surveys that have discovered NTs (e.g., E. I. Chiang et al. 2003; S. S. Sheppard & C. A. Trujillo 2006, 2010b; A. C. Becker et al. 2008; D. W. Gerdes et al. 2016; H. W. Lin et al. 2016, 2019; M. T. Bannister et al. 2018; P. H. Bernardinelli et al. 2020, 2022).

In this work, we present the very first estimates of the NT population yield within the LSST, quantifying the expected discovery numbers, characterization potential through phase and light curves, and implications for study of the NT population. Forecasting the discoveries of NTs will be vitally important in the LSST era for aiding in planning follow-up observational campaigns for, e.g., orbit refinement or spectroscopy, ensuring that the LSST is fully exploited. Such predictions will also allow for tests to be performed on NT population models—different capture and migration scenarios produce differing NT distributions, so comparison with real LSST samples will help constrain these scenarios. Knowledge

---

[18] https://www.minorplanetcenter.net/iau/lists/NeptuneTrojans.html

of the NT inclination distribution shape may help in distinguishing between capture scenarios from a widely dispersed disk with cold/hot components or a single-component, thinner-width disk (P. S. Lykawka et al. 2009; D. Nesvorný & D. Vokrouhlický 2009; A. H. Parker 2015; Y.-Y. Chen et al. 2016; H. W. Lin et al. 2021). Additionally, numerical simulations show that 3% of Centaurs may originate from formerly captured NTs, producing an additional reservoir that can be understood by measurement of the NT population (J. Horner & P. S. Lykawka 2010). Given the current lack of constraints on the NT population, the LSST's immense observational capabilities, and its imminent late-2025 commencement, it is therefore timely to estimate just how many NTs the LSST should be able to detect.

In Section 2, we describe the setup for our simulation, including a description of the LSST cadence simulation, the survey simulator `Sorcha` (M. J. Holman et al. 2025; S. R. Merritt et al. 2025), and our models for the NTs. In Section 3, we outline the major results for the NT discoveries within the decade-long operation of the LSST, including the expected timelines of discoveries and number of observations of both L4 and L5 clouds, and the light-curve and phase-curve opportunities. Section 4 looks at the predictions for discovery yields within the 3 month-long Science Validation survey. Finally, Section 5 summarizes the results and discusses factors that may influence the interpretation and scope of these findings.

2. Method

In order to estimate the NT population observable within the LSST, we set out to build a model for the NTs, as has similarly been done previously in J. A. Kurlander et al. (2025) and J. Murtagh et al. (2025), using the orbital models described in M. Alexandersen et al. (2016) and H. W. Lin et al. (2016, 2021). We use the survey simulator `Sorcha` (M. J. Holman et al. 2025; S. R. Merritt et al. 2025), combined with the most up-to-date simulation of the LSST's pointing history and model observing conditions in order to create a biased set of observations. From these, we investigate the total number of objects that are detectable within the LSST, when these objects are detectable and where on-sky these detections occur. We look to what datasets the LSST will be able to provide for phase-curve analysis, surface-color measurements, and cloud symmetry.

2.1. Sorcha

Our NT observations are simulated using the open-source, modular survey simulator `Sorcha` (M. J. Holman et al. 2025; S. R. Merritt et al. 2025). We refer the interested reader to S. R. Merritt et al. (2025) for a full discussion on the functionality of `Sorcha`, but provide a brief description here for completeness. `Sorcha` ingests an input model for the NTs, based on their orbital elements, absolute magnitudes in the r band, and optical surface colors with respect to r (as well as optional phase-curve parameters). It then generates ephemerides for all objects with its built-in N-body integrator ASSIST (M. J. Holman et al. 2023), itself an extension of REBOUND (H. Rein & S. F. Liu 2012; H. Rein & D. S. Spiegel 2015); see S. R. Merritt et al. (2025) for a list of massive perturbers used. Given a description of the Rubin Observatory (including its position, camera footprint, and realistic weather conditions), and the LSST survey itself (the filters used, the exposure times, where and when on-sky it will observe), `Sorcha` then evaluates the detectability of objects in each exposure. Detectability is determined from distance to the center of the pointing center, the exact footprint of the LSSTCam (including gaps in the CCD), removal of saturated objects, and an application of a detection efficiency function as per S. R. Chesley & P. Veres (2017). Note that initially we assume a uniform detection efficiency across the entire sky; we discuss the implications of crowded stellar fields such as the Galactic plane on NT detection in Section 3.3. After assessing object detectability, `Sorcha` then emulates the Rubin Solar System Processing (SSP) object-linking algorithm, which is designed to associate three nightly tracklets—separated by more than $5''$ spatially and less than 90 minutes temporally—within a 15 days window, all with an expected 95% linking success rate (LSST Science Collaboration et al. 2009; Z. Ivezić & The LSST Science Collaboration 2013; J. Myers et al. 2013; Ž. Ivezić et al. 2019; M. Jurić et al. 2020). The final database of detections produced by `Sorcha` can therefore be used to provide a realistic assessment of the numbers of discovered and linked objects, as well as any characterization metrics such as light curves, phase curves, or surface colors.

2.2. The LSST Cadence Simulations

Our model simulation uses the "one_snap" cadence from v4.3.1 of the observing strategy detailed in the Survey Cadence Optimization Committee (SCOC 2024) report and with a sky map of the distribution of visits in all filters shown in Figure 1. This simulation was generated by the `rubin_sim` (F. B. Bianco et al. 2022; P. Yoachim et al. 2023) and `rubin_scheduler` (E. Naghib et al. 2019; P. Yoachim et al. 2024) packages.[19] It accounts for the assumed weather conditions, optics system response (including telescope and camera performance, and mirror coating specifications), and individual filter responses (A. J. Connolly et al. 2014; F. Delgado et al. 2014; F. Delgado & M. A. Reuter 2016; P. Yoachim et al. 2016; LSST Science Collaboration et al. 2017; R. L. Jones et al. 2018, 2020; E. Naghib et al. 2019; F. B. Bianco et al. 2022). Compared to prior realizations of the cadence which employed 2 × 15 s exposures, observations are obtained in a single 29.2 s exposure (or 38 s in u) as commissioning tests of the LSSTCam have shown that cosmic-ray removal is feasible in single-visit observations. Compared to prior iterations of the cadence simulation, v4.3.1 includes an update to when the LSST will start observing in 2025 November (L. P. Guy et al. 2025). This will prove to be highly important in analyzing the detection timeline and discovery rates of the highly localized on-sky positions of the NT population. For comparison to J. Murtagh et al. (2025), we ran 100 simulations using the v4.0 cadence simulation (SCOC 2024), which has a prior assumed start date of 2025 May, as well as a redistribution in visits throughout year 1 to enable template generation. This resulted in a negligible difference in the final reported yield, only slightly affecting the timing of discoveries.

In addition to simulating the main LSST cadence, we also simulate the Science Validation (SV) survey (C. Claver et al. 2025) as also shown in Figure 1. The SV survey is an early

---

[19] For the most up-to-date cadence simulations, see https://s3df.slac.stanford.edu/data/rubin/sim-data/.

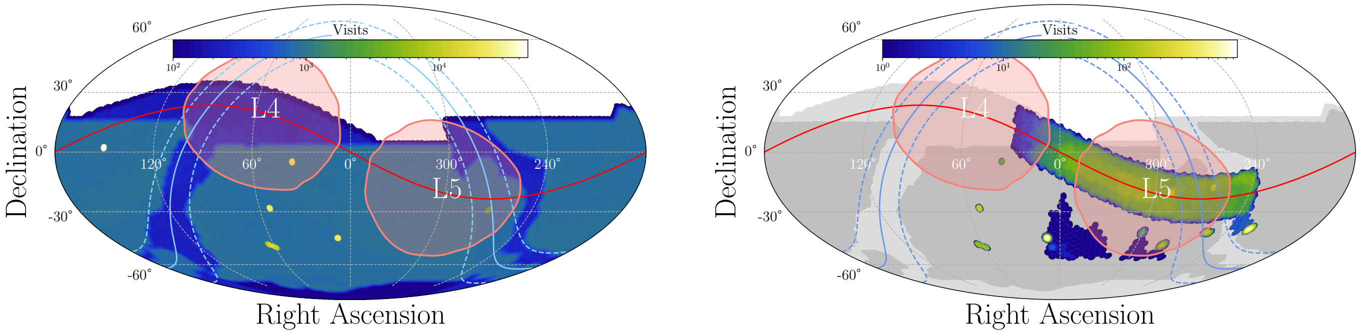

Figure 1. Sky maps of the number of visits across all filters of (left) the 10 yr LSST survey cadence based on the one-snap v4.3.1 simulation (SCOC 2024) and (right) the Science Validation survey based on the `lsstcam_20250930` simulation (C. Claver et al. 2025; NSF-DOE Vera C. Rubin Observatory 2025); note the difference in color scale between the two. The main wide-fast-deep survey makes up ∼80% of the total main LSST survey time, receiving on average ∼800 visits per pointing. Also of note are the Northern Ecliptic Spur mini-survey (dark blue region, +10° ecliptic latitude) and the Deep Drilling Fields (yellow-white circles, regions with high temporal sampling cadence). For full details of the survey strategy, see SCOC (2024). Overplotted on both in solid red is the ecliptic plane. In solid blue is the Galactic plane, with the corresponding dashed cyan lines representing ±10°. On top of all of this in pink are the positions of both L4 and L5 clouds at the beginning of the survey for context.

phase of LSST operations, commenced in 2025 June for 3 months of observing, designed to validate and refine system performance (e.g., alert generation, data release processing pipelines, solar system discovery pipelines) before full science operations commence. The overall image quality of the SV is expected to be worse than the main survey due to degraded seeing and weather conditions, with a smaller, focused $\sim 750\ \mathrm{deg}^2$ area than initially planned as a result. The simulated cadence file we use, `lsstcam_20250930` (NSF-DOE Vera C. Rubin Observatory 2025), utilizes the actual on-sky observations taken since commissioning commenced, with any non-science-grade observations removed. Simulating the SV survey allows us to assess early-year discovery probabilities under its limited and uneven footprint and understand how early coverage and cadence choices will shape the initial characterization of the NT population.

2.3. Neptune Trojan Model

Our NT model is split into three components: an orbital model consisting of semimajor axis a, eccentricity e, inclination i, libration amplitude $L_{1:1}$, argument of perihelion ω, longitude of the ascending node Ω, and mean anomaly M; a surface-color model; and a model of absolute magnitudes H with respect to the r band. We do not include any treatment for phase curves, as J. A. Kurlander et al. (2025) has shown that the distant TNO movement of ∼0°–3° in phase angle is approximately linear, and leads to minimal effects on object brightness and so observability within the LSST (see phase-curve measurements of TNOs from M. M. Dobson et al. 2023). In addition, previous NT surveys focused primarily on single-color measurements rather than phase curves of NTs (e.g., S. S. Sheppard & C. A. Trujillo 2006, 2010a; H. W. Lin et al. 2019; B. T. Bolin et al. 2023; L. Markwardt et al. 2023), and so any phase-curve parameter is poorly constrained. The input parameters for each model in this work are summarized in Table 1. We detail our absolute magnitude, color, and orbital models in the following subsections.

2.3.1. Absolute Magnitude Distribution

Determining a size distribution requires knowledge of object geometric albedo; yet for NTs, albedos are both sparsely measured (L. Markwardt et al. 2023) and may be correlated with surface color, as in other TNO populations (e.g., W. C. Fraser et al. 2014; P. Lacerda et al. 2014). Rather than introducing poorly constrained systematics, we model the absolute magnitude H distribution as a proxy for the convolution of size and albedo, which is directly measurable from survey photometry. Motivated by a growing consensus in related TNO studies, we evaluate three candidate H distributions (highlighted in Figure 2):

1. A single-component "divot" model (H. W. Lin et al. 2021) that introduces a discontinuity at a break magnitude H_B quantified by a contrast parameter c before another exponential rise. This is indicative of a population that has been "frozen-in" after being scattered from an earlier collisional environment (W. C. Fraser 2009; C. Shankman et al. 2013; M. Alexandersen et al. 2016; C. Shankman et al. 2016).
2. A two-component "divot" model (H. W. Lin et al. 2021), consisting of size-dependent "cold" and "hot" components. This distribution may reflect either a primordial two-component population captured during Neptune's migration (P. S. Lykawka et al. 2009, 2011), a single origin later split by Plutino collisions, or the emergence of a cold collisional family.
3. A rolling power law (G. M. Bernstein et al. 2004; P. H. Bernardinelli et al. 2025), whose logarithmic slope evolves smoothly via a curvature parameter θ. P. H. Bernardinelli et al. (2025) show that, for the Dark Energy Survey (DES) sample of 696 TNOs, this model can provide a common fit for all TNO dynamical and color families over the measured size range, in line with results from J.-M. Petit et al. (2023). This therefore suggests a common-origin population, similar to the color families from W. C. Fraser et al. (2023).

With only 31 H measurements recorded in the MPC, as well as previously mentioned albedo–color correlation ambiguities, the intrinsic H distribution of NTs remains effectively unconstrained, and so may be described by any of the above models. For the NTs (and other scattering objects), only a single slope H distribution has been previously disfavored by S. S. Sheppard & C. A. Trujillo (2010b), C. Shankman et al. (2013), and H. W. Lin et al. (2021) due to a deficit of intermediate-sized NTs ($H \approx 9$–11). As a result, we investigate the above three distributions in our LSST predictions in order

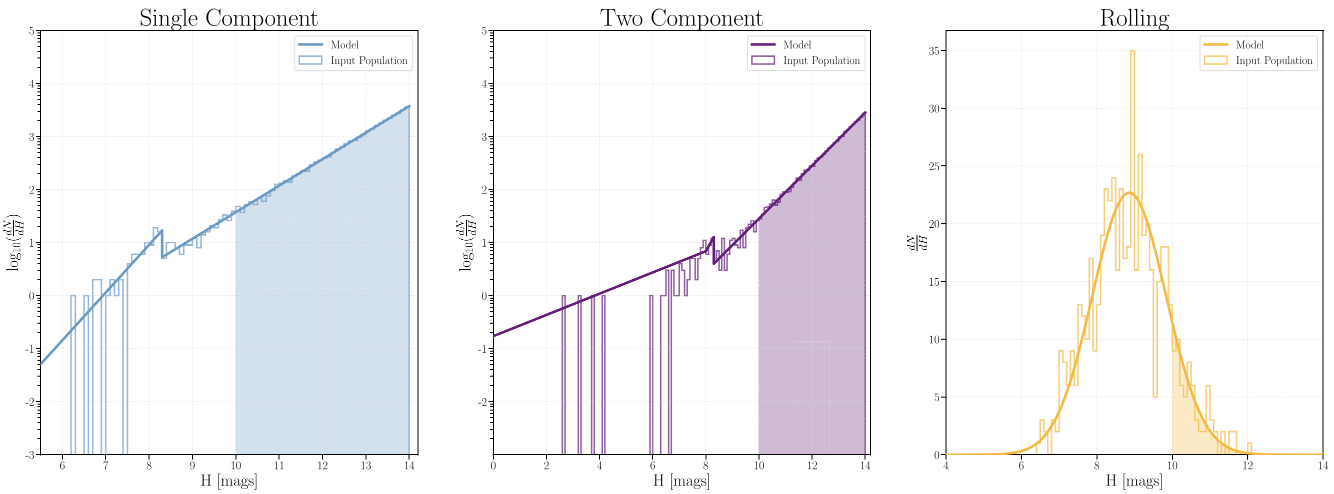

Figure 2. Differential histograms of all three absolute magnitude H distributions used in modeling the NT population in this work. In all cases, the solid line represents the analytical model for the distribution, while the histograms are the uniformly sampled $N_{\rm NT}$ objects from that model. The shaded regions in all cases represent the region beyond the LSST's nominal single-visit detection threshold ($H_r \approx 10$) for an object at Neptune's orbit. Represented here are (left panel) the single-component model, (middle) the two-component model, and (right) the rolling power-law model. Note that the single- and two-component models have a logarithmic y-axis scale, while the rolling power-law model is linear.

Table 1
Input NT Population Model Parameters for the Three Models Investigated in This Work

	Parameter	Distribution Type	Single Component	Two Component		Rolling Power Law
				Cold	Hot	
Orbits	a (au)	Uniform	30.0–30.2	30.0–30.2	30.0–30.2	30.0–30.2
	e	Rayleigh	$\sigma_e = 0.045$	$\sigma_e = 0.02$	$\sigma_e = 0.05$	$\sigma_e = 0.045$
	i (deg)	$\sin(i) \times$ Gaussian[a]	$\sigma_i = 14$	$\sigma_i = 6$	$\sigma_i = 18$	$\sigma_i = 14$
	ω (deg)	$\omega = \phi_{1:1} - M - \Omega + \lambda_N$	0–360	0–360	0–360	0–360
	Ω (deg)	Uniform	0–360	0–360	0–360	0–360
	M (deg)	Uniform	0–360	0–360	0–360	0–360
	$\phi_{1:1}$ (deg)	Equation (11)	0–360	0–360	0–360	0–360
	$L_{1:1}$ (deg)	Rayleigh	$\sigma_{L_{1:1}} = 12$	$\sigma_{L_{1:1}} = 12$	$\sigma_{L_{1:1}} = 12$	$\sigma_{L_{1:1}} = 12$
Absolute Magnitude	H_r	Power Law	Divot (0.9, 0.4, 8.3, 3.2)[b]	Single Slope (0.2, 8)[c]	Divot (0.9, 0.4, 8.3, 3.2)[b]	Rolling (0.844, −0.227)[d]
	Color Component	Mean μ		Covariance C		Mixing Weight f_α
Color[e]	NIRB[e]	$\begin{pmatrix} 0.609 & 0.223 & 0.355 \end{pmatrix}$		$\begin{pmatrix} 0.00434 & 0.00337 & 0.00547 \\ 0.00337 & 0.00268 & 0.00437 \\ 0.00547 & 0.00437 & 0.00727 \end{pmatrix}$		0.682
	NIRF[e]	$\begin{pmatrix} 0.902 & 0.347 & 0.524 \end{pmatrix}$		$\begin{pmatrix} 0.00674 & 0.00362 & 0.00557 \\ 0.00362 & 0.00205 & 0.00321 \\ 0.00557 & 0.00321 & 0.00533 \end{pmatrix}$		0.318

Notes. λ_N is Neptune's mean longitude. $\sigma_{e/i/L_{1:1}}$ are the widths of the associated distribution. They are discussed in further detail in Section 2.3.3.

[a] Truncated at 60°.

[b] (α_b, α_f, H_B, c): the bright-end slope parameter, the faint-end slope parameter, the break magnitude, and the contrast parameter, respectively.

[c] (α_1, $H_{\rm max}$): the cold component slope parameter and the cutoff magnitude, respectively.

[d] (θ, θ'): the slope curvature parameter and first derivative of the slope curvature parameter, respectively.

[e] All three absolute magnitude models share the same GMM-based color model from P. H. Bernardinelli et al. (2025). Here, NIRB is the near-infrared bright component and NIRF is the near-infrared faint component (see Section 2.3.2).

to probe a more complete range of NT size-distribution behavior. The input parameters for each H_r model are highlighted in Table 1.

To set our maximum simulated H_r value in all cases, we take the faintest recorded *griz* visit magnitudes within the v4.3.1 cadence simulation, and calculate the value of H at this apparent magnitude at 30.1 au. Each H value is converted to a H_r value using the brightest $g - r/i - r/z - r$ colors obtained from the distributions in Section 2.3.2. Finally, an additional margin of 2 magnitudes is applied in order to account for the fact that the limiting magnitude represents 50% detection efficiency, and so repeat observations of faint objects slightly fainter than the limiting magnitude may be observable with enough repeat observations. This results in a faint-end cutoff of $H_{\rm max} = 14$ for all of the distributions described below.

Single-component model. The single-component model as detailed in H. W. Lin et al. (2021) describes two single power laws separated by a "divot" component at some break magnitude H_B, with differing slopes on the bright and faint ends of the distribution. The cumulative total number of NTs for a faintest absolute magnitude $H_{\max}$ after H_B is given by the following equation (see Appendix A for a full derivation):

$$N(\leqslant H_{\max}) = \underbrace{k_b 10^{\alpha_b H_B}}_{H<H_B} + \underbrace{k_b \frac{1}{c}\frac{\alpha_b}{\alpha_f}\frac{10^{\alpha_b H_B}}{10^{\alpha_f H_B}}\left(10^{\alpha_f H_{\max}} - 10^{\alpha_f H_B}\right)}_{H\geqslant H_B}, \tag{1}$$

where k_b is a normalization constant that controls the size of the distribution, α_b/α_f are slope values for the bright and faint ends of the distribution, respectively, and c is a contrast parameter that controls the size of the postdivot drop. By performing an inverse transform of Equation (1), the number of objects to be drawn from this total distribution can therefore be assigned H values using the following equations, according to the ratio of bright end to total objects (again see Appendix A for a full derivation and determination of this ratio):

$$H = \begin{cases} \dfrac{1}{\alpha_b}(\log_{10}(\mathcal{U}) + \alpha_b H_B) & H < H_B \\ \dfrac{1}{\alpha_f}\log_{10}(\mathcal{U}\cdot(10^{\alpha_f H_{\max}} - 10^{\alpha_f H_B}) + 10^{\alpha_f H_B}) & H \geqslant H_B \end{cases}, \tag{2}$$

where $\mathcal{U}$ is a random number in the uniform distribution $\in[0, 1)$. We use values for $(\alpha_b, \alpha_f, c, H_B) = (0.9, 0.5, 3.2, 8.3)$ from H. W. Lin et al. (2021), originally determined in S. M. Lawler et al. (2018), as they have already proved to be nonrejectable best fits to OSSOS NT data using Anderson–Darling sampling tests. We use a population scaling from H. W. Lin et al. (2021), who use the Pan-STARRS1 and OSSOS+ detections with a survey simulator to estimate (assuming symmetric L4 and L5 clouds) that there are 360^{+230}_{-196} NTs with $H < 10$ (in agreement with previous estimates from H. W. Lin et al. 2019). From this, we find that the model produces $N_{\rm NT}(H < 14) = 32,472$. This model H distribution also produces $N_{\rm NT}(H < 7) = 5$ objects. While the MPC contains only one such object with $H < 7$, the apparent magnitude of such an object would approximately be $m \sim 21.7$, which is well within the LSST's nominal limiting depth of $m_r \sim 24.7$ (F. B. Bianco et al. 2022). As the survey space of NTs has been relatively limited thus far and remains incomplete at the bright end, as shown from prior Pan-STARRS1 and OSSOS+ surveys (S. S. Sheppard & C. A. Trujillo 2010b; H. W. Lin et al. 2016, 2021), combined with much larger objects existing within other resonances (e.g., Pluto with $H_V = -0.53$ in the 3:2 resonance, as per the MPC), we do not completely rule out the possibility of such future discoveries. However, we note that G. M. Bernstein et al. (2004), M. E. Brown (2008), J. M. Petit et al. (2011), J. J. Kavelaars et al. (2021), and K. J. Napier & F. C. Adams (2022) all report a potential lower size limit of $H = 5.65$ for dynamically cold objects. If applicable to NTs, this would imply that our model's prediction of zero such objects is consistent with these dynamical constraints. The resulting H distribution, after sampling $N_{\rm NT}$ many objects using Equation (2), is shown in Figure 2.

Two-component model. H. W. Lin et al. (2021) also find significant statistical evidence for a two-component H distribution of the NTs, whereby the bimodal H distribution can be described with a single power-law "cold" component and a divot power-law "hot" component as follows:

$$N(\leqslant H_{\max}) = \begin{cases} \text{Cold: } \underbrace{k_1 10^{\alpha_1 H_{\rm x}}}_{H<8} \\ \text{Hot: } \underbrace{k_b 10^{\alpha_b H_B}}_{H<H_B} + \underbrace{k_b \frac{1}{c}\frac{a_b}{a_f}\frac{10^{a_b H_B}}{10^{afH_B}}\left(10^{a_f H_{\max}} - 10^{a_f H_B}\right)}_{H\geqslant H_B} \end{cases}, \tag{3}$$

where k_1/k_b are normalization constants which control the size of the distribution for the cold and hot component, respectively, $\alpha_1/\alpha_b/\alpha_f$ are the slope values for the cold $H < 8$, hot $H < H_B$, and $H \geqslant H_B$ parts of the distribution, respectively, and c is a contrast parameter representing the size of the drop postdivot. The number of objects to be drawn from this distribution can again be assigned H values using the same inverse transform method as for Equation (1):

$$H = \begin{cases} \text{Cold: } \left\{ \dfrac{1}{a_1}(\log_{10}(\mathcal{U}) + \alpha_1 8) \quad H < 8 \right. \\ \text{Hot: } \begin{cases} \dfrac{1}{\alpha_b}(\log_{10}(\mathcal{U}) + \alpha_b H_B) & H < H_B \\ \dfrac{1}{\alpha_f}\log_{10}(\mathcal{U}\cdot(10^{\alpha_f H_{\max}} - 10^{\alpha_f H_B}) + 10^{\alpha_f H_B}) & H \geqslant H_B \end{cases} \end{cases}, \tag{4}$$

where again $\mathcal{U}$ is a random number in the uniform distribution $\in[0, 1)$.

For the cold component of this population, we use values of $(\alpha_1, \alpha_b) = (0.2, 0.9)$ as per estimates from H. W. Lin et al. (2021), who find there should be $N_{\rm cold} = N(H < 8) = 26^{+22}_{-12}$ cold NTs. For the hot component of this distribution, we again use the values of $(\alpha_b, \alpha_f, c, H_B) = (0.9, 0.5, 3.2, 8.3)$ from H. W. Lin et al. (2021) and S. M. Lawler et al. (2018) before, giving an estimate of $N(H < 10) = 272^{+168}_{-150}$. The total number of hot component NTs to simulate is thus $N_{\rm hot} = N(H < 14) = 24{,}534$. This model therefore overall produces $N_{\rm NT}(H < 14) = N_{\rm cold} + N_{\rm hot} = 24{,}560$ NTs. Similarly to the single-component model, the parameters used here produce $N_{\rm cold}(H < 7) = 16$ and $H_{\rm hot}(H < 7) = 4$ objects. We also note that the cold component yields 11 objects below the lower size limit of $H < 5.65$; however, this represents a small fraction of the discoverable population isolated in Section 3.1, and it remains unclear whether this constraint, derived from dynamically cold TNO populations, applies directly to NTs as well. The hot and cold H distributions are shown in Figure 2.

Rolling power-law model. From P. H. Bernardinelli et al. (2025), the rolling power-law formulation describes the probability for a given absolute magnitude H within two compositional surface types (excluding the Haumea collisional family), $\beta \in \{\text{NIRB,NIRF}\}$, where NIRB ("near-infrared bright") and NIRF ("near-infrared faint") refer to objects that are respectively brighter or fainter in the near-infrared at similar optical colors (see Section 2.3.2 for further discussion). The probability distribution of the rolling power-law model is given by

$$p_\beta(H|\theta_\beta,\, \theta'_\beta) \propto 10^{\theta_\beta(H-7)+\theta'_\beta(H-7)^2}, \tag{5}$$

where θ_β and θ'_β are slope curvature parameters. As in the analysis from P. H. Bernardinelli et al. (2025), we assume that the NT population shares the same rolling power-law form as all other dynamical families in the TNO population, which is reasonable given their observed inclination and eccentricity distributions. As such, we use the more simple (but still statistically strong, $\mathcal{R} = 2.370$) assumption that the posterior distributions of the NIRB/NIRF θ_β and θ'_β overlap enough to be common, with $\theta_{\mathrm{NIRB}} = \theta_{\mathrm{NIRF}} = 0.844$ and $\theta'_{\mathrm{NIRB}} = \theta'_{\mathrm{NIRF}} = -0.227$. P. H. Bernardinelli et al. (2025) restricted their analysis to their detected DES sample range of $5.5 < H < 8.2$; however, the MPC reports that the majority (18) of known NTs have measured values of $H > 8.2$. As such, we choose to extend the distribution range of Equation (5) by first normalizing by the debiased estimated number of NTs in this sample, $N_{\mathrm{NT}} = 139^{+78}_{-56}$, and the maximum posterior estimate in the original H range as follows:

$$N(<H_{\max}) = \frac{N_{\mathrm{NT}}}{\int_{5.5}^{8.2} \sum_\beta f_\beta p_\beta(H|\theta_\beta,\, \theta'_\beta) dH} \cdot \int_0^{H_{\max}} \sum_\beta f_\beta p_\beta(H|\theta_\beta,\, \theta'_\beta) dH, \tag{6}$$

where f_β are the fractions of the NT population which belong to the NIRB or NIRF types (see Section 2.3.1). Using this formulation, we find that this model produces $N_{\mathrm{NT}}(H < 14) = 556$ NTs, with $N(H < 7) = 15$ and $N(H < 10) = 488$. We uniformly sample by interpolating the cumulative distribution function of this distribution with a cubic spline fit via the `scipy.interpolate.interp1d` function, resulting in the H distribution shown in Figure 2. The large discrepancy in N_{NT} compared to the single- and two-component H models is due to the power-law index rolling over to zero at $H \approx 9$ (see performing a Taylor expansion of the power term in Equation (5)), resulting in the slope *decreasing* after this. While this has the potential caveat of underestimating the faint end of the NT distribution, there are not yet enough measurements to confidently constrain this distribution. With the sample size available from S. S. Sheppard & C. A. Trujillo (2010b), C. J. Shankman (2012) note that the NT size distribution is consistent within 2σ with negative slopes for $H > 9$, in line with the turnover of this rolling power-law distribution. Furthermore, at the LSST's limiting magnitude of $m_r \sim 24.7$, an object at 30.1 au would correspond to $H_r \approx 10$, indicating that the range considered here is adequately probing the magnitude range in which the LSST is expected to discover NTs.

2.3.2. Colors

TNOs, including NTs, exhibit a pronounced color bimodality, commonly partitioned into "red" and "very red" groups, which likely reflect compositional gradients in the primordial protoplanetary disk (W. C. Fraser & M. E. Brown 2012; C. M. Dalle Ore et al. 2013; M. E. Schwamb et al. 2019; L. E. Buchanan et al. 2022; W. C. Fraser et al. 2023; M. Marsset et al. 2023; R. E. Pike et al. 2023). In particular, the optical and near-infrared colors of NTs are of interest due to their dynamically stable and collisionally unevolved status (W. F. Bottke et al. 2023), making them potentially direct tracers of the disk's original chemical stratification. Recently, W. C. Fraser et al. (2023) formalized these color distinctions into near-infrared-bright (BrightIR) and near-infrared-faint (FaintIR) classes, defined by their relative brightnesses in optical and near-infrared J-band colors, again thought to correspond to distinct primordial surface materials. Building on this framework, P. H. Bernardinelli et al. (2025) modeled the joint color distribution of the entire DES sample (696 TNOs, including six NTs) as a two-component Gaussian mixture model (GMM; we refer the reader to P. H. Bernardinelli et al. 2025 for a full treatment of their GMM modeling process). These components, which they refer to as NIRF and NIRB, defined by their relative i/z-band brightnesses at fixed $g - r$ colors, are seen to closely mirror the FaintIR and BrightIR populations in W. C. Fraser et al. (2023), respectively, as well as being consistent with recent James Webb Space Telescope spectral groupings of TNOs and NTs (L. Markwardt et al. 2025). We adopt their GMM parameterization to describe our NT color distribution: For a measurement $\boldsymbol{x} = (g - r,\, r - i,\, r - z)$, the color distribution it is drawn from is modeled as a weighted sum of multivariate Gaussians $\mathcal{N}$:

$$p(\boldsymbol{x}|\boldsymbol{\mu}_\alpha,\, \boldsymbol{C}_\alpha) = \sum_{\alpha=1}^{K} f_\alpha \mathcal{N}(\boldsymbol{x}|\boldsymbol{\mu}_\alpha,\, \boldsymbol{C}_\alpha) \times \left(\text{where}\, \mathcal{N}(\boldsymbol{x}|\boldsymbol{\mu}_\alpha,\, \boldsymbol{C}_\alpha) \equiv \frac{1}{\sqrt{(2\pi)^3|\boldsymbol{C}_\alpha|}} \times e^{-\frac{1}{2}(\boldsymbol{x}-\boldsymbol{\mu}_\alpha)^{\mathrm{T}}\boldsymbol{C}_\alpha^{-1}(\boldsymbol{x}-\boldsymbol{\mu}_\alpha)}\right), \tag{7}$$

where $\boldsymbol{\mu}_\alpha/\boldsymbol{C}_\alpha$ are the mean and covariance of the αth Gaussian of the model, weighted by f_α (such that $\sum_\alpha f_\alpha = 1$). From this, we utilize their estimate of the mean and covariances of the best-fit GMM output (highlighted in Table 1), and fraction of NTs in the NIRF class (obtained from a sample size of six NTs) of $f_{\mathrm{NIRB}} = 0.682 \pm 0.156$ for our color model. We then select N_{NT} samples uniformly from this GMM distribution (where N_{NT} is the number of NTs in a given model population; see Appendix B for an explanation of the implementation of multivariate normal sampling), ensuring that correlation in color is maintained in each selection. The resulting model color distributions are shown in Figure 3.

We note that we do not model u/y-band colors, motivated by J. A. Kurlander et al. (2025), who showed that u-band observations contribute negligibly to TNO discoveries, while y-band observations provide only marginal improvements, with no Y-band observations of NTs seen within the comparable DES sample (P. H. Bernardinelli et al. 2022, 2023). Given that NT colors are expected to resemble those of other TNO populations (B. T. Bolin et al. 2023; L. Markwardt et al. 2023), and that the L4 cloud remains predominantly within the NES region (where only *griz* observations occur), this simplification has minimal impact on our color characterization results and effectively provides a conservative lower limit on expected yields. We also note that no NT has been discovered with a $g - r \approx 0.75$ within the NIRF class,

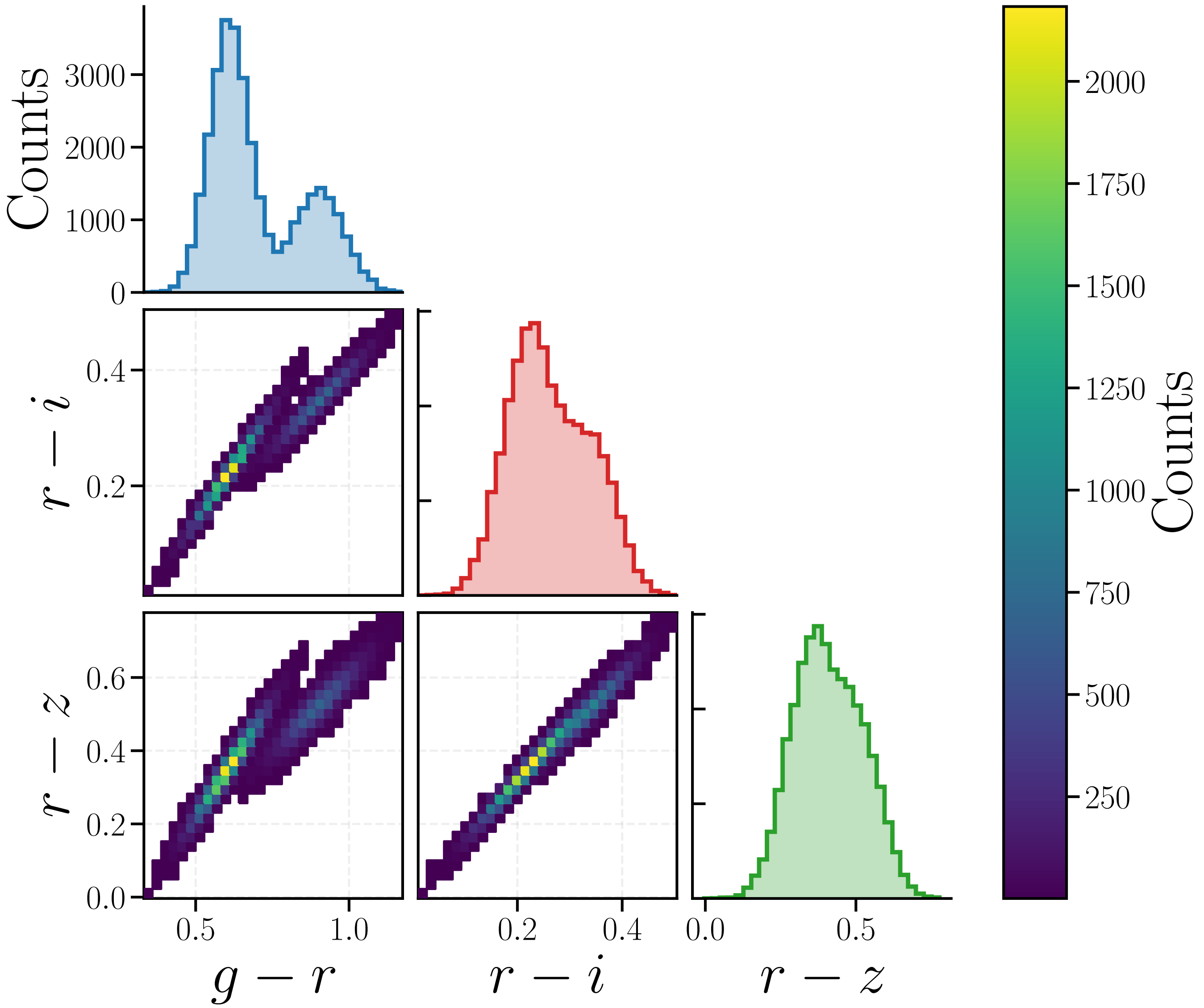

Figure 3. $g-r$, $r-i$, and $r-z$ color histograms for the input model produced from GMM parameters in Table 1. The leading diagonal represents the individual 1D histograms of each color, while the middle-left, bottom-left, and bottom-middle 2D histograms highlight their correlation. Samples are drawn to ensure this correlation is kept.

corresponding to the spectral “double-dip” type described in N. Pinilla-Alonso et al. (2025) and surveyed in L. Markwardt et al. (2025). However, we again note that, with their sample size of eight objects, this observed dearth may be due to a lack of observations.

2.3.3. Orbital Distribution

Our NT orbital model is based on those employed in M. Alexandersen et al. (2016) and H. W. Lin et al. (2016, 2021). Both the eccentricity e and libration amplitude $L_{1:1}$ follow Rayleigh distributions as follows:

$$p(e) \propto e \cdot \exp\left(-\frac{1}{2}\left(\frac{e}{\sigma_e}\right)^2\right)de, \tag{8}$$

$$p(L_{1:1}) \propto L_{1:1} \cdot \exp\left(-\frac{1}{2}\left(\frac{L_{1:1}}{\sigma_{L_{1:1}}}\right)^2\right)dL_{1:1}, \tag{9}$$

where $\sigma_e/\sigma_{L_{1:1}}$ represent the widths of the respective Rayleigh distributions. For the single-component and rolling power-law models, we take these parameters to be the bootstrapped $\sigma_e = 0.045/\sigma_{L_{1:1}} = 12°$ values from the Pan-STARRS1/OSSOS NT observations from H. W. Lin et al. (2021). For the rolling power-law model specifically, we adopt the same single-component dynamical widths because the rolling H distribution from P. H. Bernardinelli et al. (2025) is derived under the assumption of a single underlying population and does not introduce, test for, or provide evidence of distinct hot/cold orbital components within the NTs. Thus, no separate eccentricity distributions are motivated for this case. For the two-component model, we take the bootstrapped $\sigma_e = 0.02$ for the cold component and $\sigma_e = 0.05$ for the hot component from H. W. Lin et al. (2021, both in line with other estimates from resonant populations; A. A. S. Gulbis et al. 2010; B. Gladman et al. 2012; R. E. Pike et al. 2015; M. Alexandersen et al. 2016), and $\sigma_{L_{1:1}} = 12°$ for both. We note that previous studies have shown that for $e > 0.12$ and $L_{1:1} > 35°$, tadpole orbits are no longer stable, and are instead indicative of metastable, or even transient captures (D. Nesvorný & D. Vokrouhlický 2009; L.-Y. Zhou et al. 2009; A. H. Parker 2015). As we are only simulating on the timescale of the decade-long survey, and not investigating a purely primordial capture scenario, we choose to probe the full range of $e/L_{1:1}$ to explore the effects of such temporary captures on detections.

The inclination i distribution is modeled as a truncated sin (i) × Gaussian distribution (M. E. Brown 2001) as follows:

$$p(i) = \begin{cases} \sin(i) \cdot \exp\left(-\frac{1}{2}\left(\frac{i}{\sigma_i}\right)^2\right) & i < i_t \\ 0 & i \geqslant i_t \end{cases}, \qquad (10)$$

where σ_i is the width of the Gaussian distribution and i_t is the truncation inclination, set at $i_t = 60°$ (see H. W. Lin et al. 2021) and in line with the reasonable survey coverage extent of the LSST. R. Malhotra & S. Roy (2023), I. C. Matheson et al. (2023), and P. H. Bernardinelli et al. (2025) have shown that a von Mises–Fisher (N. I. Fisher et al. 1993) distribution may provide greater statistical significance for modeling the inclination distributions of various TNO dynamical families. However, the concentration parameter κ that controls the concentration of the distribution around the mean is poorly measured for NTs; P. H. Bernardinelli et al. (2025) were unable to satisfactorily constrain the correlation with NIRB/NIRF class using the six NTs within the DES sample. As such, we opt to use the simpler Brown distribution instead, as the width σ_i was not observed to have any additional color dependency in the analysis of H. W. Lin et al. (2021). For the single-component and rolling power-law models, we again use the bootstrapped inclination width from H. W. Lin et al. (2021) of $\sigma_i = 14°$, while for the two-component model we have $\sigma_{i,\text{cold}} = 6°$ and $\sigma_{i,\text{hot}} = 18°$. For the rolling power-law model, we retain the single-component σ_i from H. W. Lin et al. (2021) because the rolling power-law H distribution of P. H. Bernardinelli et al. (2025), while containing separate NIRB/NIRF photometric classes, does not identify or require distinct dynamical inclination or eccentricity widths for NTs.

For all models, our semimajor axis distribution is uniformly distributed in the range $\mathcal{U} \in [30.0\text{ au}, 30.2\text{ au}]$, or ±0.1 au from Neptune's semimajor axis value of ~30.1 au (a <1% variation, which M. Alexandersen et al. 2016 note that on this scale has little effect on NT detectability). The longitude of the ascending node Ω and mean anomaly M distributions are all sampled from a continuous uniform distribution $\mathcal{U} \in [0°, 360°)$ for all models to account for the effects of orbital precession due to interactions with the giant planets. The resonance argument $\phi_{1:1}$, which controls the split of L4 and L5 clouds, is evenly distributed for all models between the libration centers ~60° and ~300° by the formula

$$\phi_{1:1} = \left(\frac{\pi}{3} + R \cdot \frac{2\pi}{3} + L_{1:1}\sin(2\pi \cdot u)\right) \bmod 2\pi, \qquad (11)$$

where $R \in \{-1, 0\}$ and u is uniformly sampled from the continuous distribution $\in [0, 1)$. Finally, the argument of perihelion ω is computed from the resonance condition $\omega = \phi_{1:1} - \Omega - M + \lambda_N$, where λ_N is Neptune's mean longitude, ensuring that $\phi_{1:1}$ is not independent of the orbital angles but still satisfies the required 1:1 resonant geometry. The resulting orbital distributions in $a/e/i$ for all three models are shown in Figure 4, with $L_{1:1}/\phi_{1:1}$ shown in Figure 5.

3. LSST Predictions

The results presented here are based on the median outcomes of 1000 simulations for each absolute magnitude H_r model described in Section 2.3.1. For each run, a new NT population model was randomly drawn following the procedure in Section 2.3 and ran through `Sorcha`. The resulting spread corresponds to uncertainties of ~21%, ~20%, and ~11% in the discovery yield, illustrated by the shaded regions in Figure 6. To evaluate the sensitivity of the yield to model assumptions, we also performed additional simulations varying the population scaling parameters (Section 2.3.1) and the color class fractions f_{NIRB} (Section 2.3.2). The scaling parameter variations, shown in Appendix C, vary the final yields by $^{+82\%}_{-65\%}$, $^{+81\%}_{-63\%}$, and $^{+55\%}_{-55\%}$ for the single-component, two-component, and rolling power-law models, respectively. By contrast, varying the color class fractions has only a negligible impact, shifting the total yield by at most ±~3 objects. For the remainder of this section, we present results using the best-estimate values for each model parameter.

3.1. Neptune Trojan Discovery Yield

The per-Lagrange cloud cumulative 10 yr survey discoveries of NTs within the LSST are shown in Figure 6, with yield totals at 1, 2, 5, and 10 yr summarized in Table 2. Applying a uniform detection efficiency across the whole sky for difference imaging (the true detection efficiency performance of the LSST is still unknown; see Section 3.2 for the effects of the Galactic plane), we find 146^{+34}_{-29} single-component, 133^{+28}_{-25} two-component, and 285^{+37}_{-30} rolling power-law NTs discovered. The higher yield in the rolling power law arises from the steeper slope of the bright end of the distribution ($H_r < 8.3$) than the other models, leading to approximately double the intrinsic number of objects here that the LSST can easily detect. Compared to the 31 NTs known within the MPC, these yields therefore represent a ~fourfold to ninefold increase in the known population. The current largest individual survey samples of new NT discoveries are the eight discovered in the DES (D. W. Gerdes et al. 2016; H. W. Lin et al. 2019; P. H. Bernardinelli et al. 2020, 2022), six discovered in the survey of S. S. Sheppard & C. A. Trujillo (2010a), five discovered in Pan-STARRS1 (H. W. Lin et al. 2016), and the five in OSSOS+ (M. T. Bannister et al. 2018). The large leap in NT discoveries compared to prior dedicated NT surveys is owed to the LSST's ability not only to perform relatively narrow, deep searches like prior surveys, but to tile the entire L4 and L5 cloud regions to depths of $m_r \sim 24.7$ (Ž. Ivezić & The LSST Science Collaboration 2013; F. B. Bianco et al. 2022) multiple times over 10 yr. This enables a less biased approach to NT population studies, probing a more complete magnitude and spatial range of the NTs.

Of each total yield, the discoveries are split in an approximately 1:2 ratio between L4 to L5 cloud NTs, respectively; this ratio may change if our initial assumption of symmetric clouds is not accurate. This imbalance arises purely from on-sky localization and survey cadence, and is summarized in Figure 7. From the start of the survey the L4

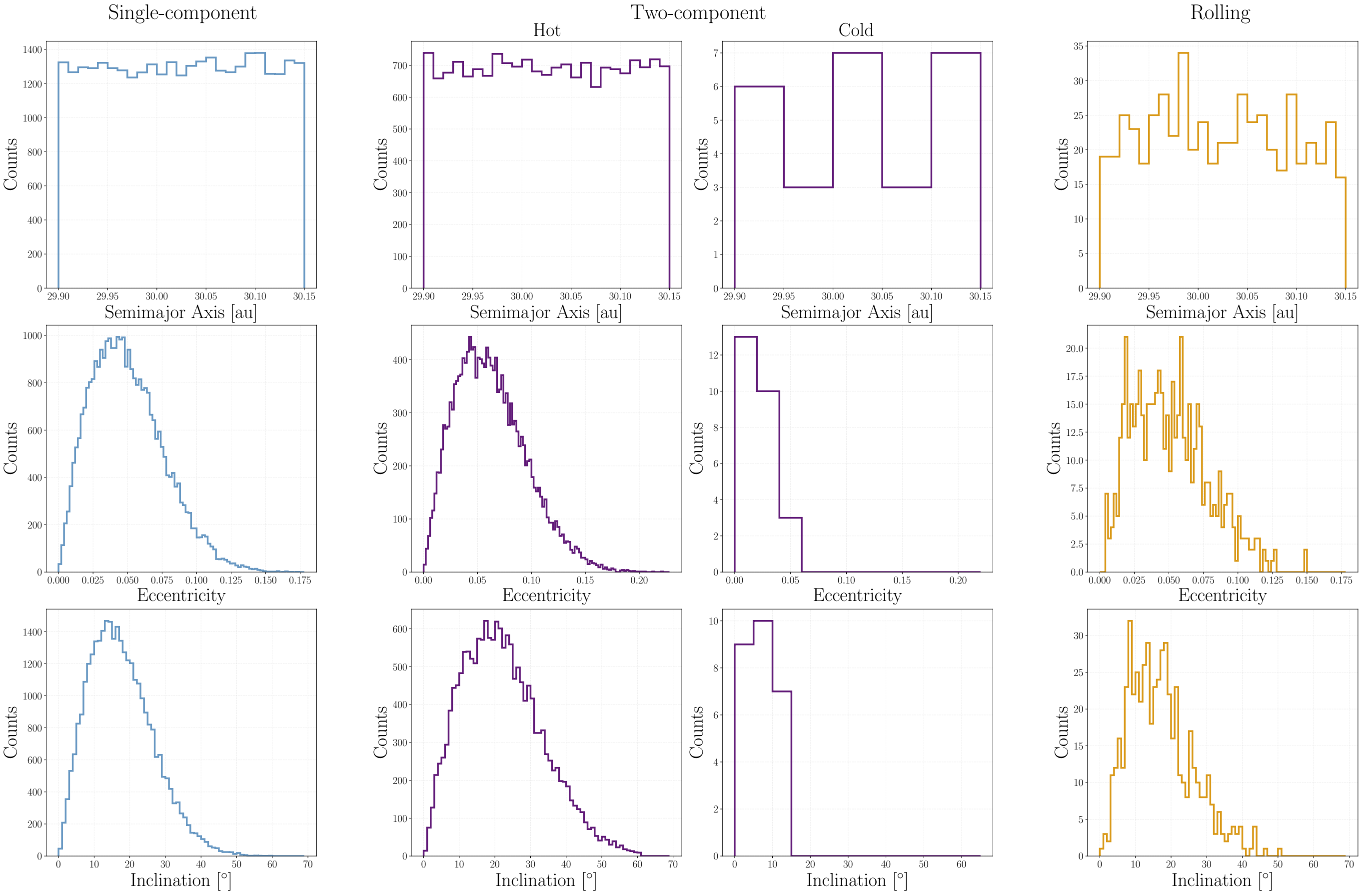

Figure 4. Orbital distributions in (top row) semimajor axis a, (middle row) eccentricity e, and (bottom row) inclination i for the (left column) single-component, (middle column) two-component, and (right column) rolling power-law models, respectively.

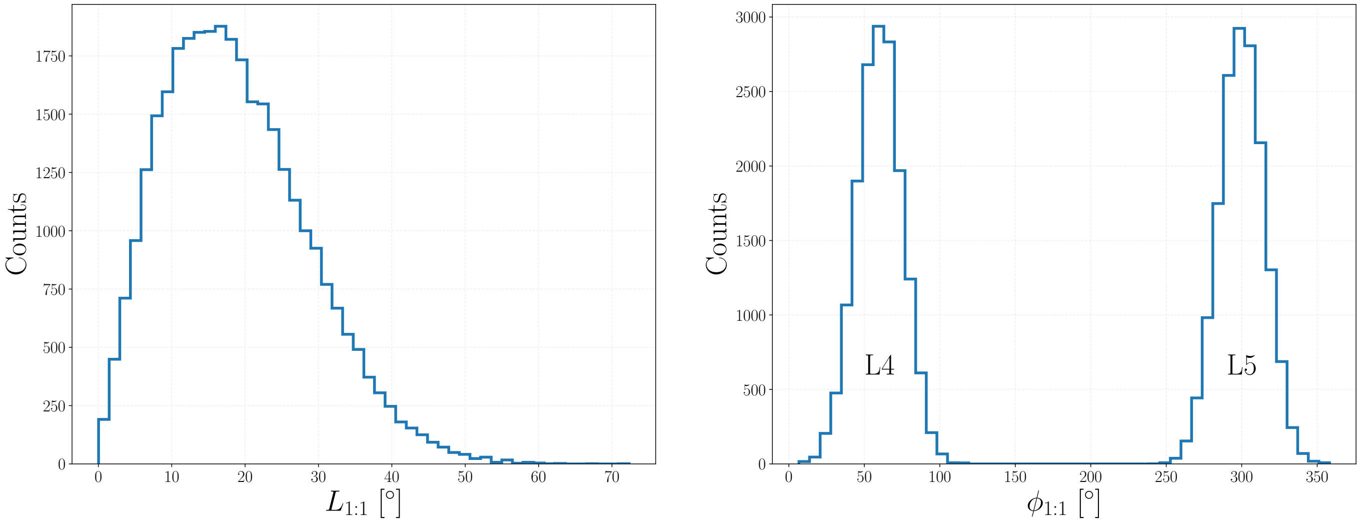

Figure 5. Example distributions of libration angle $L_{1:1}$ and resonance argument $\phi_{1:1}$ used for all three H models. All three models share the same distribution shapes for $L_{1:1}$ and $\phi_{1:1}$, differing only in the number of objects sampled from them.

cloud resides predominantly within the comparatively more sparsely covered NES region (see Figure 1), while the L5 cloud remains fully within the WFD footprint over the full survey duration. This is further reflected in Figure 6, where discoveries of L5 NTs are delayed compared to L4, until the cloud becomes observable within the main survey. Historically, the L5 cloud's proximity to the Galactic plane has made discovery difficult, due to crowded stellar fields hindering difference imaging (e.g., S. S. Sheppard & C. A. Trujillo 2010a). The LSST therefore offers an unprecedented opportunity to systematically measure the L5 cloud in order to constrain the true L4:L5 population ratios, whose (a)symmetry has direct implications for their initial dynamical capture mechanism (S. S. Sheppard & C. A. Trujillo 2010a).

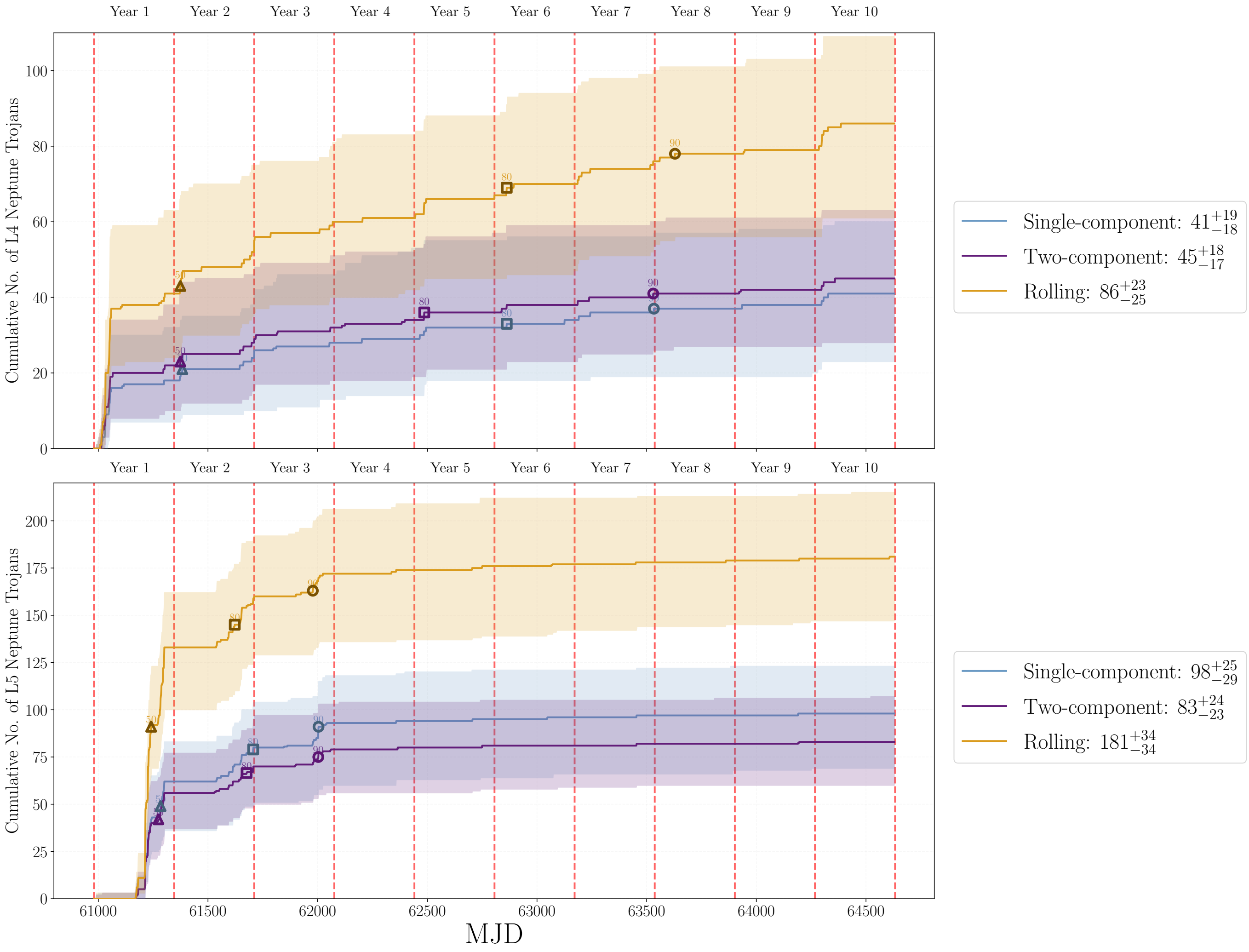

Figure 6. Cumulative histogram (with a bin size of 1 day) of the discovery rates over the 10 yr LSST lifetime for the single-component (blue), two-component (purple), and rolling power-law (orange) models. These are further split by (top row) L4 discoveries and (bottom row) L5 discoveries, with L5 discovery delayed until the cloud is observable in the survey. The points of 50% (open triangle), 80% (open square), and 90% (open circle) completion are shown for each model. Red dashed vertical lines represent survey year start/end points. The pronounced plateau in year 1 discoveries corresponds to an early surge of L4 detections, followed by a lull until sky rotation brings the L5 cloud into an observable airmass.

Table 2
Number of Neptune Trojan Discoveries by Survey Year for Each Absolute Magnitude Model and Split by Lagrange Cloud

Lagrange	Model	LSST Discovery Numbers			
		1 yr	2 yr	5 yr	10 yr
L4	Single component	18	24	32	41
	Two component	22	28	36	45
	Rolling	41	52	66	86
L5	Single component	62	80	95	98
	Two component	56	70	81	83
	Rolling	133	159	176	181
Combined	Single component	80	104	127	139
	Two component	78	98	117	128
	Rolling	174	211	242	267

Note. As a reference, the MPC only notes 31 Neptune Trojans, with 27 in L4 and four in L5.

Our simulations show that, irrespective of the NT model, the LSST will discover approximately half of its 10 yr NT yield within year 1 (Figure 6). This rapid early surge is dominated by the brightest objects, with the mean apparent r-band magnitude at first detection being $m_r \sim 22.7$. By the second year, this decreases by about 1 magnitude to an average of $m_r \sim 23.7$, approaching the LSST's nominal single-visit limiting magnitude ($m_r \sim 24.7$; Z. Ivezić & The LSST Science Collaboration 2013; F. B. Bianco et al. 2022). Beyond this time, discoveries are governed by fainter objects moving inwards, and so becoming bright enough to obtain repeat observations that allow them to pass tracklet linkage thresholds for the SSP pipeline. This trend reflects how the LSST's long-term, wide-area coverage enables the eventual recovery of such faint objects, in contrast to prior surveys that were limited to objects bright enough for discovery at time of observation (S. S. Sheppard & C. A. Trujillo 2010b).

The final differential distributions of both the apparent and absolute magnitudes at the end of the survey are highlighted in Figure 8. Detections are cut off at $H_r = 5.65$ to isolate NTs that are more likely to have been captured from local primordial material (G. M. Bernstein et al. 2004; M. E. Brown 2008; J. M. Petit et al. 2011; J. J. Kavelaars et al. 2021; K. J. Napier & F. C. Adams 2022). Of the 31 NTs listed in the MPC, only seven have a $H_V \geqslant 9.0$, with the faintest at $H_V = 10.2$.

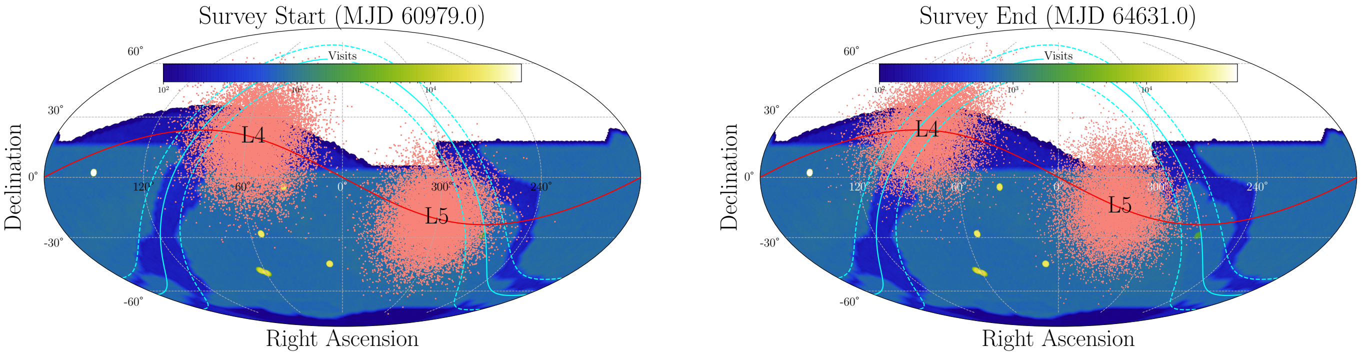

Figure 7. Sky coverage of an entire input intrinsic NT orbital model (pink scatter points) at the beginning of the survey (left) vs. at the end of the survey (right) showing the bulk movement of the underlying clouds. In both projections, the L4 cloud is labeled on the left, whereas the L5 cloud is labeled on the right. The red solid line shows the ecliptic plane, and the light blue line the Galactic plane with dashed lines marking ±10° off of it.

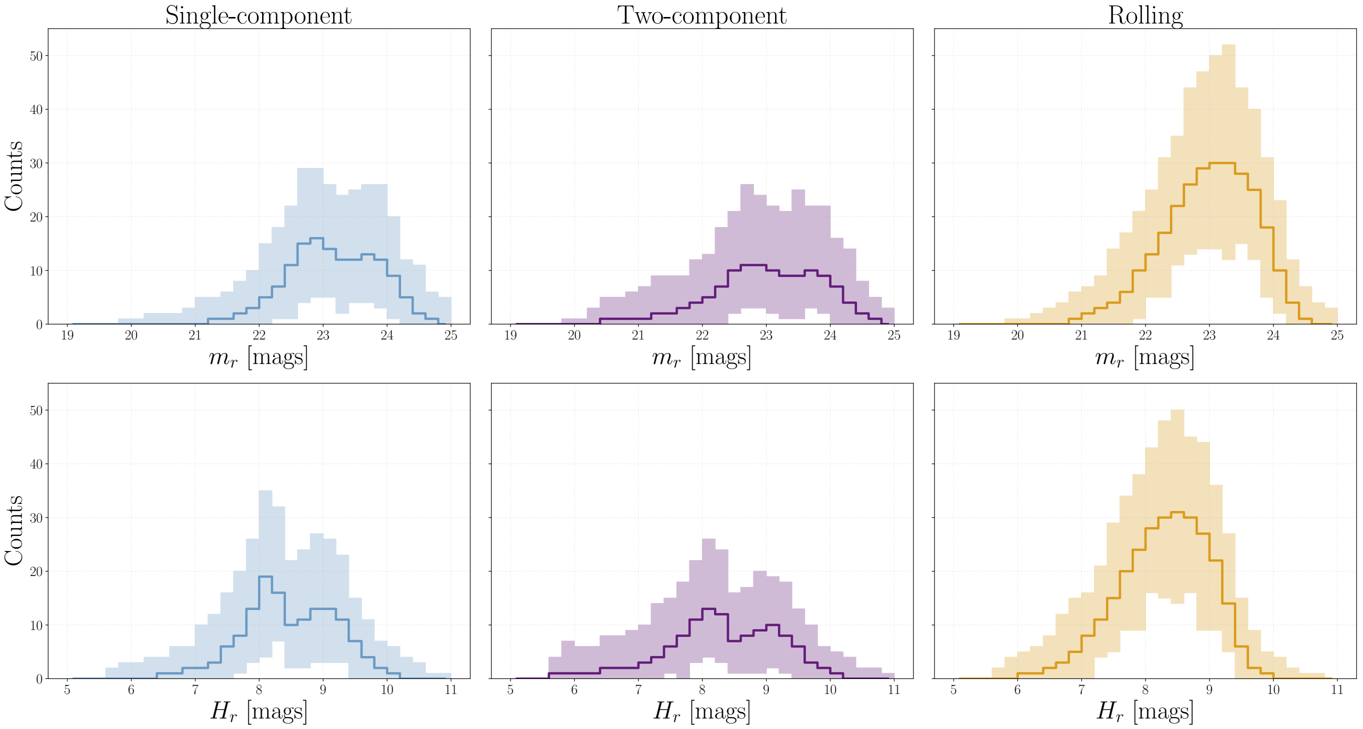

Figure 8. Final 10 yr differential histograms of (top row) the median apparent magnitude distribution in the r band at the time of linkage of detected NTs for the three input models, and (bottom row) the median absolute magnitude in the r band of all detected NTs. The shaded region in each panel represents the uncertainty on all 10^3 simulations.

The LSST NT sample will push this to a depth of $H_V \approx 10.2$–11.2 (assuming $V - r = 0.2$; see Jupiter Trojans; H. W. Lin et al. 2021), probing NT sizes down to ∼15 km (assuming a 5% albedo; again see Jupiter Trojans; Y. R. Fernández et al. 2003, 2009; S. S. Sheppard & C. A. Trujillo 2010b). More importantly, we predict the LSST will discover ∼70–130 NTs brighter than the break magnitude $H_B = 8.3$ and ∼60–150 fainter, compared to the 13 and 18 known in the MPC, respectively. The LSST will thus ensure coverage well into both the large and small regimes of the size–frequency distribution; statistics of bright/large NTs, where the slope reflects the primordial population size distribution, can be used to directly compare NT capture mechanism models (A. Morbidelli et al. 2009), whereas faint/small NTs will allow for probing the commensurability with other dynamically hot TNO families (W. C. Fraser et al. 2014). Crucially, this H range spans a region sensitive to long-term collisional evolution (W. F. Bottke et al. 2023), which will assist in discrimination between a slope shaped by direct capture of NTs versus one modified by Gyr-scale collisional grinding.

3.2. Galactic Plane Observations

The high stellar densities within ±10° of the Galactic plane (G. Gilmore & N. Reid 1983; B. Chen et al. 2001; M. Jurić et al. 2008; E. Valenti et al. 2016) can make NT discovery more difficult due to overlapping and blending of the star/NT point-spread functions, and the resulting challenge of generating reliable sky templates that accurately subtract stellar backgrounds for difference imaging (K. A. G. Olsen et al. 2003; J. Kubica et al. 2007). While our baseline simulations assume perfect difference-imaging capability, real observations within the Galactic plane will inevitably suffer reduced single-visit efficiency. To quantify the impact, we removed all

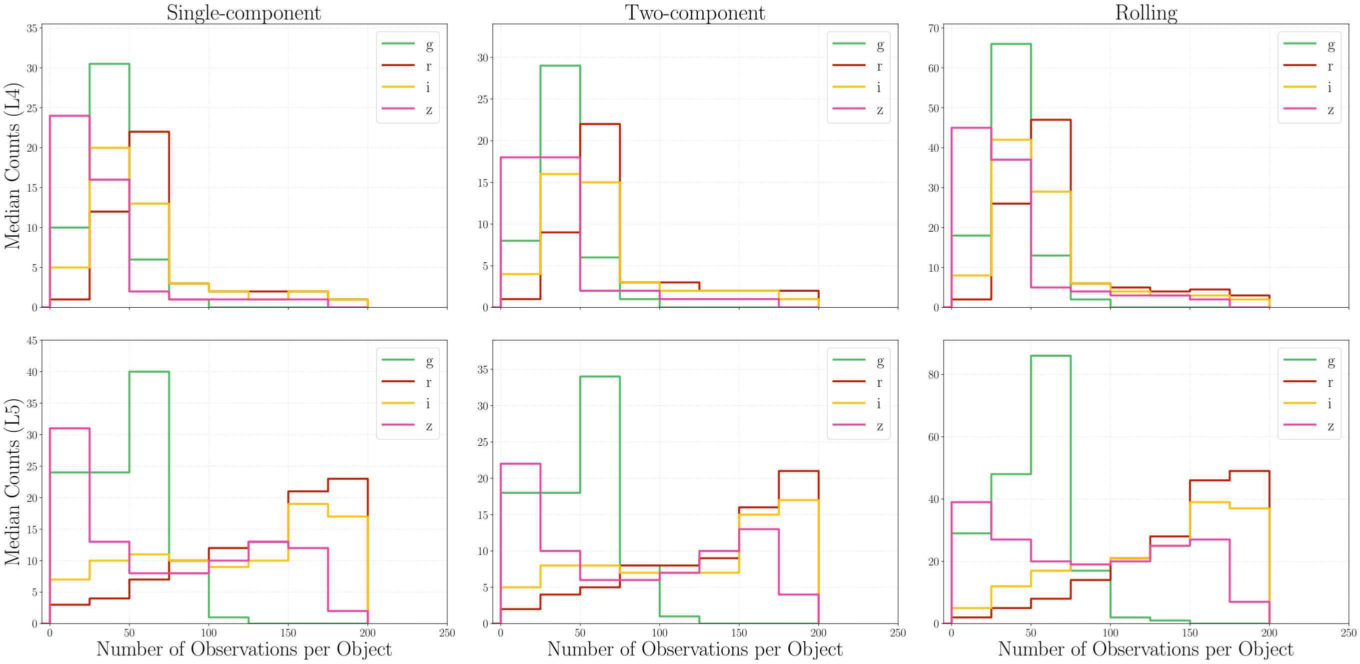

Figure 9. Histograms of the number of detections per object, broken down per filter for the three input models (columns) and by Lagrange cloud (L4, top row; L5, bottom row). All exclude any observations that fall within a DDF.

observations within ±10° of the Galactic plane from the v4.3.1 cadence simulation, and reran our models. This excision only reduced the total NT yield by ~15%, and the median number of observations per object by ~8% for all models, providing a lower limit on NT yields; this minimal impact is largely due to the L5 cloud moving away from the plane during the survey, whereas the L4 cloud, residing primarily in the NES region, receives less visits overall than the L5 within the WFD region (see Figure 7). We however also provide a more nuanced approach to NT detection by applying an empirical detection efficiency penalty derived from the search for NTs in high-stellar-density fields by S. S. Sheppard & C. A. Trujillo (2010a). This produces an even smaller effect, reducing the initial cadence scenario by <1% and instead slightly shifting discoveries to survey cadence periods not within the plane. These results indicate that the Galactic plane has minimal long-term impact on the LSST's NT yield: Bright objects in the plane still accumulate sufficient detections over the 10 yr survey to meet linking thresholds, even if single-visit performance is temporarily degraded.

3.3. Observation Numbers and Orbit Arcs

Over the 10 yr baseline, each detected NT in our simulations accumulates ~240–290 observations per object, excluding DDF visits, assuming that the SSP linking behavior performs to expected efficiency (M. Jurić et al. 2020) and that precovery (i.e., recovering observations of the object postlinkage) is possible. From LSST observations alone, >95% are observed for approaching the full survey duration, giving them orbital arcs >9 yr. The long, dense arcs that the LSST by itself can provide here will be more than adequate at lowering orbital uncertainties enough to distinguish between the 1:1 resonance from other nearby ones (or other scattering populations), and allow for accurate long-term orbit integrations to calculate libration amplitude to classify NTs as stable or metastable within the resonance. In our sample, the contamination from potentially transient or metastable objects is small, with ~10 NTs with $e > 0.12/L_{1:1} > 35°$, indicating that these should not affect primordial population studies significantly.

Due to the spatial extents of the L4 and L5 clouds, entrance into any of the DDF areas is exceedingly rare—over 10^3 simulations, on average no NTs ever enter either the COSMOS ($150^{\mathrm{h}}06^{\mathrm{m}}36^{\mathrm{s}}/+02^{\mathrm{d}}13^{\mathrm{m}}48^{\mathrm{s}}$), or the X-ray Multi-Mirror Mission Large Scale Structure (XMM-LSS, hereafter XMM; $35^{\mathrm{h}}34^{\mathrm{m}}12^{\mathrm{s}}/-04^{\mathrm{d}}49^{\mathrm{m}}12^{\mathrm{s}}$), with a maximum of three L4 NTs within XMM in any simulation. Those few L4 NTs that do pass through XMM remain for about a year, and receive at least twice the number of total observations across all filters as a WFD-only NT. Population-wide NT studies will thus come from WFD discoveries; however, if any do enter XMM, with ~250 observations for single- and two-component NTs and ~290 for rolling power-law NTs, they will allow for dense light-curve coverage and detailed case studies on photometric variability.

3.4. Light Curves and Colors

The LSST's cadence will also provide rich per-object coverage across all filters, with the distribution in visits per filter, separated by Lagrange cloud, shown in Figure 9, and summarized in Table 3; the bimodality in $r/i/z$-band observations that is not seen in g is a reflection of the input NT model being intrinsically less bright in g, combined with the WFD L5 NTs being observed ~2–3 more times on average than NES L4 NTs, producing bimodality in the brighter $r/i/z$ bands. The average signal-to-noise ratio (S/N) per object is ~40–70, or a magnitude uncertainty of ~0.015–0.025 mag. With average observations of 15–30 per object per year, and given the ability to observe both clouds, the LSST will enable the first comprehensive NT light-curve study, probing the similarity of photometric variability relative to the wider TNO population to better constrain their origin (D. Jewitt 2018), and expanding the color sample from prior surveys (S. S. Sheppard & C. A. Trujillo 2006;

Table 3
Median Number of Detections of NTs, for All Observations Irrespective of Filter, and Split across Filters over the 10 yr LSST Survey Duration (Excluding DDF Visits)

Lagrange	Model	Median Number of Observations per Object				
		All Filters	g	r	i	z
L4	Single component	165	36	55	48	25
	Two component	176	37	57	52	29
	Rolling	169	36	55	49	26
L5	Single component	389	50	148	127	64
	Two component	427	54	156	139	79
	Rolling	440	56	159	143	83

B. T. Bolin et al. 2023; L. Markwardt et al. 2023). While the survey cadence and use of multiple broadband filters is particularly suited for long-term monitoring and color sampling of objects, the long inter-night visit gaps per filter ($\sim$week(s); R. L. Jones et al. 2014; F. B. Bianco et al. 2022) may limit rotation sensitivity to longer periods. Nevertheless, a broad population-level study will still be possible.

In order to investigate the number of NTs that will have a well-measured color light curve, we apply the quality metrics as defined in M. E. Schwamb et al. (2023), as derived from the LSST Metrics Analysis Framework (R. L. Jones et al. 2014). These metrics require that, for a given object, at least one band (primary) has >30 observations, and all other (secondary) bands have >20, each with a $\mathrm{S/N} > 5$. Physically, this is intended to provide a proxy for fitting a light curve in the primary band and to use the secondary bands to refine the fit and improve color measurements; however, for objects with less photometric variability, these metrics may not be feasible. Applying these metrics to our dataset yields $\sim$60% of NTs ($\approx$ 87, 80, and 171 for the single-component, two-component, and rolling power-law models, respectively) that pass the criteria—a slight increase on the TNOs from J. A. Kurlander et al. (2025), but broadly attributable to our model containing proportionally more relatively bright objects. On the lowest estimate, this sample more than quadruples the sample size used in the surveys from B. T. Bolin et al. (2023; 18), L. Markwardt et al. (2023; 15), and D. Jewitt (2018; 13). A quadrupled sample size with precisely measured surface colors from phase-curve fitting will allow the LSST to more accurately measure the exact red/very red color fraction (B. T. Bolin et al. 2023), and directly test the tentative absolute magnitude–color correlation reported by L. Markwardt et al. (2023). These objects will also supply many well-characterized targets for spectroscopic follow-up to probe red/very red compositional differences (L. Markwardt et al. 2025).

4. Science Validation Survey Predictions

While the main survey will ultimately dominate NT discoveries, the interim SV survey (see Section 2.2) will offer a unique preview of the LSST's early NT yield. Simulating observations with the `lsstcam_20250930` cadence, and assuming perfect template generation for difference imaging, we predict median discovery yields over 10^3 simulations of 33^{+18}_{-15}, 32^{+14}_{-16}, and 72^{+34}_{-21} for the single-component, two-component, and rolling power-law models, respectively. The survey's limited coverage and cadence is overwhelmingly biased toward observing the L5 cloud (see Figure 7), with $<2\%$ of discoveries coming from the L4 cloud. Across these simulated detections, individual objects receive a median of $\sim$30 visits, broken down into four g, 10 r, eight i, and six y observations per filter, providing a rich dataset for preliminary photometric variability and color measurements. All simulated detections occur before 2025 September 21, the end of the real observations included in the final SV database. This means the simulated discovery samples correspond entirely to epochs already captured on-sky, implying that the SV dataset may already contain counterparts to many of the NTs predicted here. These represent potential viable NT candidates awaiting identification in the existing images within Data Preview 2 (L. P. Guy et al. 2025).

5. Conclusions

In this work, we have combined the current best understanding of the NT orbital and surface-color models together with the survey simulator `Sorcha` and a cadence simulation of the LSST in order to produce the very first estimates for the observability of the NTs in the LSST. With its unprecedented depth, cadence, and sky coverage, we find that the LSST will usher in a new era of NT science, characterized by the following:

1. The predicted number of NT discoveries within the LSST is 146, 133, and 285 for single-component, two-component, and rolling power-law model absolute magnitude distributions, respectively. This represents a $\sim$fourfold to ninefold increase on the known 31 NTs within the MPC dataset today.
2. There is a bias toward discovery and observation of L5 NTs over L4 NTs, despite an intrinsically symmetric cloud distribution, due to the L4 residing predominantly within the lower-cadence NES region of the LSST survey footprint. The L5 cloud has historically been understudied however, due to its proximity to the high-stellar-density Galactic plane, so the LSST will here offer the first opportunity to systematically investigate any (a)symmetries between the two.
3. Removing Galactic plane observations altogether from our simulations only reduces the yield of each model by $\sim$15%, approximately the same level as the uncertainty due to simulation randomization. Objects which are bright enough will still accumulate sufficiently high-S/N observations over the 10 yr survey to pass linking thresholds regardless (assuming idealized SSP performance).
4. Nearly all of each NT model ($>95\%$) will achieve orbital arcs >9 yr, allowing for well-constrained orbit measurements to confirm stability within the 1:1 resonance.
5. Of each NT model, 60% pass quality color light-curve metrics, giving at least a fourfold increase on the color samples used in previous color studies, allowing for more robust tests of absolute magnitude–color correlations and red/very red color population fractions.

While the results presented in this work provide a detailed forecast for NT detections in the LSST era, they remain dependent on several key assumptions that warrant caution. Chief among these is the small sample size from which our input models are drawn: Current constraints on the absolute magnitude distributions are based on fewer than 30 known objects, most of which reside in the L4 cloud (H. W. Lin et al. 2021). The underlying population parameters, particularly the size distributions, therefore carry substantial uncertainties. We have quantified this by running 1000 simulations, yielding an estimated uncertainty of ±10%–23% due to simulation randomization, absolute magnitude scaling uncertainties of $^{+82\%}_{-65\%}$, $^{+81\%}_{-63\%}$, and $^{+55\%}_{-55\%}$ for the single-component, two-component, and rolling power-law models, respectively (see Appendix C), and a color uncertainty of ±1%–2%. Yet even under the most conservative yield estimate, in the two-component model, the known NT population size is set to quadruple from the known MPC population.

Further caveats include assumptions made regarding the template generation process. Our simulation assumes static, pregenerated templates are available for all sky regions prior to survey commencement, which does not reflect reality. M. E. Schwamb et al. (2023) and J. E. Robinson et al. (2025) discuss in detail the impact that such a lack of template generation will have on year 1 statistics for solar system objects; although real-time discoveries may vary due to this, observations will remain recoverable as incremental template generation proceeds and data are reprocessed for Data Release 1 (L. P. Guy et al. 2025). Our modeled detection efficiency also presumes idealized performance from the SSP pipelines; in practice however, linking efficiency, false-positive rates, and tracklet fitting performance may reduce the effective yield, particularly in lower-cadence regions like the NES, or high-stellar-background regions like the Galactic plane. Finally, the precise commencement date of observing with the LSST will also have an effect on observation numbers due to continuous movement of the clouds placing them in better or worse alignment with regions like the DDFs. If the LSST were to start observations later than 2025 November, this would result in further drift of both clouds, affecting their observability and potentially altering our yield estimates.

Despite these uncertainties, our results reinforce the exceptional potential for the LSST to revolutionize NT science. With detections extending to magnitudes approaching $m_r \sim 24$, and arc lengths of approximately a decade for most objects, the LSST will enable detailed orbital classification, population modeling, and physical characterization—particularly for the underexplored L5 cloud. The breadth and depth of the anticipated data signal the beginning of a statistically robust era in outer solar system dynamics, capable of addressing longstanding questions on the origin and evolution of this 1:1 resonant population.

Acknowledgments

J.Mu. acknowledges support from the Department for the Economy (DfE) Northern Ireland postgraduate studentship scheme and travel support from the Science and Technology Facilities Council (STFC) for UK participation in LSST through grant No. ST/S006206/1. J.Mu. and J.A.K. thank the LSST-DA Data Science Fellowship Program, which is funded by LSST-DA, the Brinson Foundation, and the Moore Foundation; their participation in the program has benefited this work. M.E.S. acknowledges support in part from STFC UK grant Nos. ST/V000691/1 and ST/X001253/1. P.H.B., J.A.K., M.J., P.Y., J.Mu., and C.O.C. acknowledge the support from the University of Washington College of Arts and Sciences, Department of Astronomy, and the Data-intensive Research in Astrophysics and Cosmology (DiRAC) Institute. The DiRAC Institute is supported through generous gifts from the Charles and Lisa Simonyi Fund for Arts and Sciences, Janet and Lloyd Frink, and the Washington Research Foundation. M.J.H. gratefully acknowledges support from the NSF (grant No. AST2206194) and the NASA YORPD Program (grant No. 80NSSC22K0239). S.C. acknowledges that this work was supported in part by the Department of Education through the Graduate Assistance in Areas of National Need Fellowship Program award P200A240010 at the University of Illinois Department of Aerospace Engineering.

This research has made use of NASA's Astrophysics Data System Bibliographic Services. This research has made use of data and/or services provided by the International Astronomical Union's Minor Planet Center. The SPICE Resource files used in this work are described in C. H. Acton (1996) and C. Acton et al. (2018). Simulations in this paper made use of the REBOUND *N*-body code (H. Rein & S. F. Liu 2012). The simulations were integrated using IAS15, a 15th-order Gauss–Radau integrator (H. Rein & D. S. Spiegel 2015). Some of the results in this paper have been derived using the `healpy` and HEALPix packages. This work made use of Astropy (https://www.astropy.org/): a community-developed core `Python` package and an ecosystem of tools and resources for astronomy (Astropy Collaboration et al. 2013, 2018, 2022). We thank the Vera C. Rubin Observatory Data Management Team and Scheduler Team for making their software open source. This research received support through Schmidt Sciences.

We are grateful for the use of the computing resources from the Northern Ireland High Performance Computing (NI-HPC) service funded by EPSRC (EP/T022175).

We thank the anonymous reviewer for their helpful comments; their insight has improved this manuscript.

Software: Sorcha (M. J. Holman et al. 2025; S. R. Merritt et al. 2025), ASSIST (M. J. Holman et al. 2023; H. Rein et al. 2023), Astropy (Astropy Collaboration et al. 2013, 2018), CMasher (E. van der Velden 2020), Healpy (K. M. Górski et al. 2005; A. Zonca et al. 2019), Jupyter Notebook (T. Kluyver et al. 2016) Matplotlib (J. D. Hunter 2007), Numba (S. K. Lam et al. 2015), Numpy (C. R. Harris et al. 2020), Pandas (W. McKinney 2010; The pandas development team 2020), Pooch (L. Uieda et al. 2020), PyTables (PyTables Developers Team 2002), REBOUND (H. Rein & S. F. Liu 2012; H. Rein & D. S. Spiegel 2015), rubin_sim (F. B. Bianco et al. 2022; P. Yoachim et al. 2023), rubin_scheduler (E. Naghib et al. 2019; P. Yoachim et al. 2024), sbpy (M. Mommert et al. 2019), SciPy (P. Virtanen et al. 2020), seaborn (M. L. Waskom 2021), spacerocks (K. J. Napier 2020), Spiceypy (A. Annex et al. 2020), sqlite (https://www.sqlite.org/index.html), sqlite3 (https://docs.python.org/3/library/sqlite3.html), tqdm (C. da Costa-Luis et al. 2023).

Author Contributions

J.Mu. was responsible for writing and submitting the manuscript. He ran all of the simulations and performed all of the analysis detailed in this manuscript.

M.E.S. supervised and contributed to the overall discussion and conception of the initial research concept. She provided meaningful edits and proofreads to this manuscript.

P.H.B. contributed to the development and design of the models used within this work, including provision of original curated data and code. He also provided meaningful edits and proofreads of this manuscript.

H.W.L. contributed to the initial research concept and provided original curated code to develop the models used within this work. He also provided meaningful edits and proofreads of this manuscript.

J.A.K. provided the initial plotting scripts to produce sky maps in Figures 1 and 7.

G.F. and M.J.H. provided meaningful edits and proofreads of the manuscript and contributed significantly to the development of the survey simulator `Sorcha` used in this work.

R.L.J. and P.Y. produced the cadence simulations of the Rubin Observatory used within this work.

S.R.M., S.C., M.J., S.E., J.Mo., J.K., D.O., M.W., and C.O. C. all contributed significantly to the development of the survey simulator `Sorcha` used in this work.

Appendix A
Deriving the Divot Power Law

A broken (or "knee") power law describes a distribution whose slope changes abruptly at some break value, often used to model size–frequency distributions of small bodies. A divot variant additionally includes a multiplicative drop in number density at some break value, producing a discontinuity between the slopes either side. From C. J. Shankman (2012), the differential form of the "divot" power law in an infinitesimal absolute magnitude H range is given by

$$\frac{dN}{dH} = \begin{cases} k_b \alpha_b \ln(10) 10^{\alpha_b H} \\ \left(\text{where } k_b = A \cdot 10^{-\alpha_b H_0}\right) \end{cases} H < H_B, \tag{A1a}$$

$$\frac{dN}{dH} = \begin{cases} k_f \alpha_f \ln(10) 10^{\alpha_f H} \\ \left(\text{where} \quad k_f = B \cdot 10^{-\alpha_f H_B}\right) \end{cases} H \geqslant H_B, \tag{A1b}$$

where $k_b/k_f$are normalization parameters (with constants A/B) for the "bright" and "faint" ends of the distribution with respect to an observationally determined normalization absolute magnitude H_0 and the break absolute magnitude H_B, respectively. α_b/α_f are the slope parameters of the bright and faint ends of the distribution. This is shown diagrammatically in Figure A1. The cumulative total number of objects after the break magnitude $N(< H_B)$ is found by the sum of the integrals of the bright and faint components of the distribution over the appropriate pre- and postbreak magnitude ranges, respectively.

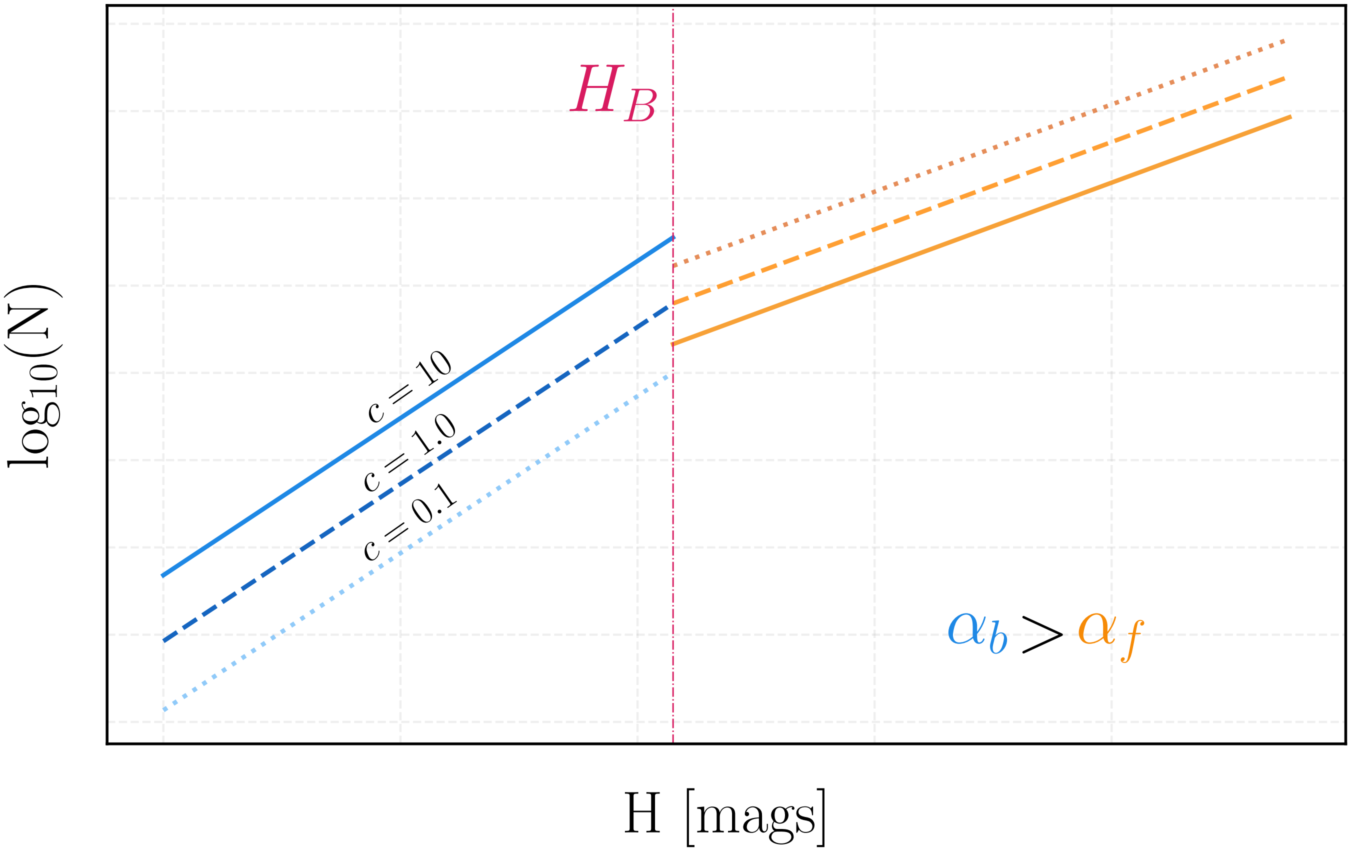

Figure A1. Graphical representation of the differential power law. The "bright" end of the distribution (blue) is quantified by a slope α_b, whereas the "faint" end (orange) is quantified by a slope α_f (in this plot, $\alpha_b > \alpha_f$), with a break at H_B. The size of the divot at H_B is quantified by a contrast parameter c, that is the ratio of the differential binned objects predivot to the differential binned objects postdivot. For $c = 1.0$ (dashed), the power law reduces to a broken "knee" form, whereas for $c < 1$ and $c > 1$, a "divot" power law occurs, either increasing (dotted) or decreasing (solid) the number of objects postbreak, respectively.

Integrating first Equation (A1a):

$$\begin{aligned} N(<H_B) &= \int_{-\infty}^{H_B} dN \\ &= \int_{-\infty}^{H_B} k_b\alpha_b \ln(10) 10^{\alpha_b H} dH \\ &= k_b\alpha_b \ln 10 \frac{1}{\alpha_b \ln(10)}\, 10^{\alpha_b H}\Big|_{\infty}^{H_B} \qquad \text{(A2)} \\ &= k_b \left[10^{\alpha_b H_B} - \cancelto{=0}{10^{-\infty}}\right] \\ &= k_b 10^{\alpha_b H_B} \end{aligned}$$

Now integrating the "faint" end of the distribution:

$$\begin{aligned} N(H_B \leqslant H \leqslant H') &= \int_{H_B}^{H'} dH \\ &= \int_{H_B}^{H'} k_f \alpha_f \ln(10) 10^{\alpha_f H} dH \\ &= k_f \alpha_f \ln(10) \frac{1}{\alpha_f \ln(10)} 10^{\alpha_f H} \Big| \\ &= k_f \left[10^{\alpha_f H'} - 10^{\alpha_f H_B}\right]. \end{aligned} \qquad \text{(A3)}$$

Both components are matched at the divot according to a ratio of the infinitesimal number of objects before the divot to after the divot, quantified by the contrast parameter c. The faint-end normalization parameter k_f can therefore be rewritten in terms of the bright-end normalization parameter k_b as follows:

$$\begin{aligned} N_{\text{bright}}(H = H_B) &= c \cdot N_{\text{faint}}(H = H_B) \\ k_b \alpha_b \ln(10) 10^{\alpha_b H_B} &= c \cdot k_f \alpha_f \ln(10) 10^{\alpha_f H_B} \\ k_f &= k_b \frac{1}{c} \frac{\alpha_b}{\alpha_f} \frac{10^{\alpha_b H_B}}{10^{\alpha_f H_B}}. \end{aligned} \qquad \text{(A4)}$$

Inserting this expression of k_f into Equation (A3) gives

$$\begin{aligned} N(H_B \leqslant H \leqslant H') = k_b \frac{1}{c} \frac{\alpha_b}{\alpha_f} \frac{10^{\alpha_b H_B}}{10^{\alpha_f H_B}} \\ \times \left[10^{\alpha_f H'} - 10^{\alpha_f H_B}\right]. \end{aligned} \qquad \text{(A5)}$$

Therefore, the cumulative total number of objects after the break with an arbitrary $H = H'$ is given as the sum of Equations (A3) and (A5):

$$\begin{aligned} N(\leqslant H') = \underbrace{k_b 10^{\alpha_b H_B}}_{H<H_B} \\ \underbrace{+ k_b \frac{1}{c} \frac{\alpha_b}{\alpha_f} \frac{10^{\alpha_b H_B}}{10^{\alpha_f H_B}} \left[10^{\alpha_f H'} - 10^{\alpha_f H_B}\right]}_{H \geqslant H_B}. \end{aligned} \qquad \text{(A6)}$$

If the measured $H_0 \geqslant H_B$, the value of k_B can be determined by rearranging Equation (A6) and solving using the known $N(H < H_0)$; otherwise, if $H_0 < H_B$, the value of k_b must be determined by solving the bright-end distribution, Equation (A3).

Once the normalization parameter k_b is determined, in order to uniformly draw from this distribution, one draws from the two distributions over their respective H ranges such that they contain an appropriate fraction of objects described simplifying Equation (A5) by factorizing Equation (A3) out as follows:

$$\begin{aligned} N(\leq H') = N_{total} &= k_b 10^{\alpha_b H_B} + k_b \frac{1}{c} \frac{\alpha_b}{\alpha_f} \frac{10^{\alpha_b H_B}}{10^{\alpha_f H_B}} \\ &\quad \times \left[10^{\alpha_f H'} - 10^{\alpha_f H_B}\right] \\ &= k_b 10^{\alpha_b H_B} + k_b 10^{\alpha_b H_B} \frac{1}{c} \frac{\alpha_b}{\alpha_f} \\ &\quad \times \left[10^{\alpha_f (H'-H_B)} - \cancelto{=1}{10^{\alpha_f (H_B - H_B)}}\right] \\ &= N_b \left(1 + \frac{1}{c} \frac{\alpha_b}{\alpha_f} \left(10^{\alpha_f (H'-H_B)} - 1\right)\right) \\ \frac{N_b}{N_{total}} &= \left(1 + \frac{1}{c} \frac{\alpha_b}{\alpha_f} \left(10^{\alpha_f (H'-H_B)} - 1\right)\right)^{-1} \end{aligned} \qquad \text{(A7)}$$

In order to uniformly draw from each distribution, one creates an inverse transform of the cumulative distribution functions described Equations (A3) and (A5) such that $N(<H)^{-1}(\mathcal{U})$, where $\mathcal{U}$ is uniformly distributed in the range $\in[0, 1]$. Taking the bright end first:

$$\begin{aligned} F(H) &= \frac{\cancel{k_b \alpha_b \ln(10)} \int_{-\infty}^{H'} 10^{\alpha_b H} dH}{\cancel{k_b \alpha_b \ln(10)} \int_{-\infty}^{H_B} 10^{\alpha_b H} dH} \\ &= \frac{10^{\alpha_b H'} - \cancelto{=0}{10^{-\infty}}}{10^{\alpha_b H_B} - \cancelto{=0}{10^{-\infty}}} \\ &= \frac{10^{\alpha_b H'}}{10^{\alpha_b H_B}} = \mathcal{U} \\ 10^{\alpha_b H'} &= \mathcal{U} \cdot 10^{\alpha_b H_B} \\ \alpha_b H' &= \log_{10}(\mathcal{U}) + \alpha_b H_B \\ H' &= \frac{1}{\alpha_b} \left(\log_{10}(\mathcal{U}) + \alpha_b H_B\right) \end{aligned} \qquad \text{(A8)}$$

Now inverting the faint end:

$$\begin{aligned} F(H) &= \frac{\cancel{k_f \alpha_f \ln(10)} \int_{H_B}^{H'} 10^{\alpha_f H} dH}{\cancel{k_f \alpha_f \ln(10)} \int_{H_B}^{H_{\max}} 10^{\alpha_f H} dH} \\ &= \frac{10^{\alpha_f H'} - 10^{\alpha_f H_B}}{10^{\alpha_f H_{\max}} - 10^{\alpha_f H_B}} = \mathcal{U} \\ 10^{\alpha_f H'} &= \mathcal{U} \cdot \left[10^{\alpha_f H_{\max}} - 10^{\alpha_f H_B}\right] \\ &\quad + 10^{\alpha_f H_B} \\ \alpha_f H' &= \log_{10}(\mathcal{U} \cdot \left[10^{\alpha_f H_{\max}} - 10^{\alpha_f H_B}\right] \\ &\quad + 10^{\alpha_f H_B}) \\ H' &= \frac{1}{\alpha_f} \log_{10}(\mathcal{U} \cdot \left[10^{\alpha_f H_{\max}} - 10^{\alpha_f H_B}\right] + 10^{\alpha_f H_B}) \end{aligned} \qquad \text{(A9)}$$

One can now draw N_{total} number of objects from the bright and faint distributions combined according to the fraction determined in Equation (A8). The differential, cumulative, and

Table A1
Summary of the Differential, Cumulative, and Inverse Transforms of the Divot Power Law

	$H < H_B$	$H \geqslant H_B$
Differential	$k_b \alpha_b \ln(10)\, 10^{\alpha_b H}$	$k_f \alpha_f \ln(10)\, 10^{\alpha_f H}$
Cumulative	$k_b 10^{\alpha_b H}$	$k_f \frac{1}{c}\frac{\alpha_b}{\alpha_f} 10^{\alpha_b H_B}(10^{\alpha_f (H - H_B)} - 1)$
Inverse transform	$\frac{1}{\alpha_b}(\log_{10}(\mathcal{U}) + \alpha_b H_B)$	$\frac{1}{\alpha_f}\log_{10}(\mathcal{U} \cdot (10^{\alpha_f H_{\max}} - 10^{\alpha_f H_B}) + 10^{\alpha_f H_B})$

Note. $k_b = A \cdot 10^{-\alpha_b H_0}$, bright-end normalization parameter; $k_f = B \cdot 10^{-\alpha_f H_B}$, faint-end normalization parameter; α_b/α_f, bright/faint-end slope parameter; c, slope parameter (ratio of number of objects in infinitesimally small bin prebreak to number of objects in infinitesimally small bin postbreak); H_B, break absolute magnitude; H_0, normalization absolute magnitude; H_{max}, largest absolute magnitude to draw from; $\mathcal{U}$, uniform distribution $\in [0, 1]$.

inverse transforms for the bright-end and faint-end distributions are summarized in Table A1.

Appendix B
Sampling from a Multivariate Normal Distribution for Multiple Component Gaussian Mixture Models

Sampling from a multivariate normal distribution with a given mean $\boldsymbol{\mu}$ and covariance $\boldsymbol{C}$ (i.e., $\boldsymbol{X} \sim \mathcal{N}(\boldsymbol{\mu}, \boldsymbol{C})$) is a straightforward implementation of the `numpy.random.multivariate_normal` function. In the case of Gaussian Mixture Modeling, however, where there may be K normal distributions within the overall target distribution to sample from, this function is not able to parse >1D $\boldsymbol{\mu}$ and >2D $\boldsymbol{C}$ arrays. In this instance, we instead first sample from a standard multivariate normal $\boldsymbol{Z} \sim \mathcal{N}(\boldsymbol{0}, \boldsymbol{I})$, where $\boldsymbol{I}$ is the identity matrix. As the sample distribution $\boldsymbol{X}$ is simply an affine-transformed version of the sample distribution $\boldsymbol{Z}$, we can transform between the two by

$$\boldsymbol{X} = \boldsymbol{A}\boldsymbol{Z} + \boldsymbol{\mu},$$

where $\boldsymbol{A}$ is a transformation matrix that satisfies the relation $\boldsymbol{C} = \boldsymbol{A}\boldsymbol{A}^T$ (this arises from the fact that $\boldsymbol{C} = \mathrm{cov}[\boldsymbol{X}] = \mathbb{E}[(\boldsymbol{X} - \boldsymbol{\mu})(\boldsymbol{X} - \boldsymbol{\mu})^T] = \boldsymbol{A}\mathbb{E}[\boldsymbol{Z}\boldsymbol{Z}^T]\boldsymbol{A}^T = \boldsymbol{A}\boldsymbol{I}\boldsymbol{A}^T = \boldsymbol{A}\boldsymbol{A}^T$). The transformation matrix $\boldsymbol{A}$ can be found via Cholesky decomposition of the covariance matrix $\boldsymbol{C}$ (where $\boldsymbol{A}$ is a lower triangle matrix whose elements are all real and whose diagonal elements are positive), which is implemented via the `numpy.linalg.cholesky` function. This entire sampling method is wrapped in the GMM analysis code used in P. H. Bernardinelli et al. (2025), and is publicly available for open use on GitHub.[20]

Appendix C
Yield Range for Absolute Magnitude Uncertainties

The yields for each NT absolute magnitude models is shown in Figure C1, with the range on each representing the upper and lower estimate for the scaling parameters used in constructing each model (see Section 2.3.1). Table C1 breaks down the yield per year for both the upper and lower estimates for years 1, 2, 5, and 10 of the LSST operations.

---

[20] https://github.com/bernardinelli/gmm_anyk

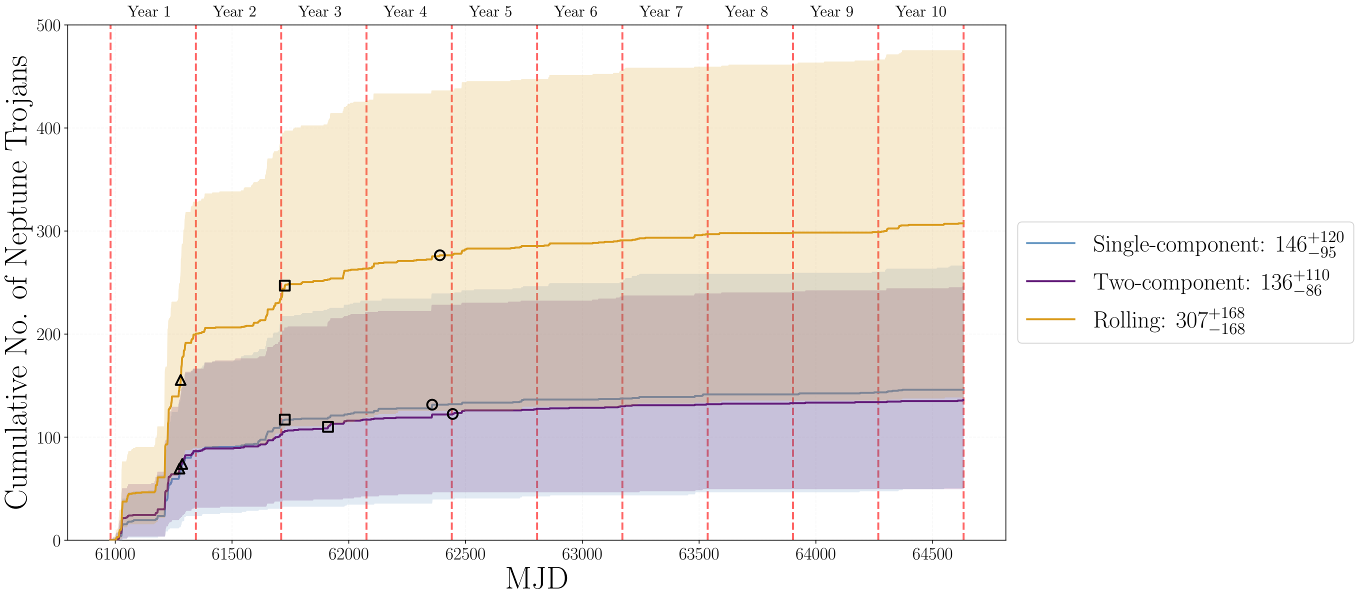

Figure C1. Cumulative histogram (with a bin size of one day) of the discovery rates over the 10 yr LSST lifetime for the single-component (blue), two-component (purple), and rolling power-law (orange) models. The points of 50% (open triangle) 80% (open square), and 90% (open circle) completion are shown for each model. Red dashed vertical lines represent survey year start/end points. The ranges here represent the upper and lower estimate for the scaling parameters used in each model, described in Section 2.3.1.

Table C1
Number of Neptune Trojan Discoveries by Survey Year for the Lower and Upper Limit from Each Absolute Magnitude Model's Scaling Parameter Described in Section 2.3.1

		LSST Discovery Numbers			
		1 yr	2 yr	5 yr	10 yr
Upper estimate	Single-component	166	211	246	266
	Two-component	166	194	232	246
	Rolling	328	384	447	475
Lower estimate	Single-component	24	32	43	51
	Two-component	32	38	47	50
	Rolling	90	105	130	139

Note. As a reference, the Minor Planet Center only notes 31 Neptune Trojans.

ORCID iDs

Joseph Murtagh https://orcid.org/0000-0001-9505-1131
Megan E. Schwamb https://orcid.org/0000-0003-4365-1455
Pedro H. Bernardinelli https://orcid.org/0000-0003-0743-9422
Hsing Wen Lin (林省 文) https://orcid.org/0000-0001-7737-6784
Jacob A. Kurlander https://orcid.org/0009-0005-5452-0671
Stephanie R. Merritt https://orcid.org/0000-0001-5930-2829
Samuel Cornwall https://orcid.org/0000-0002-0672-5104
Mario Jurić https://orcid.org/0000-0003-1996-9252
Grigori Fedorets https://orcid.org/0000-0002-8418-4809
Matthew J. Holman https://orcid.org/0000-0002-1139-4880
Siegfried Eggl https://orcid.org/0000-0002-1398-6302
R. Lynne Jones https://orcid.org/0000-0001-5916-0031
Peter Yoachim https://orcid.org/0000-0003-2874-6464
Joachim Moeyens https://orcid.org/0000-0001-5820-3925
Jeremy Kubica https://orcid.org/0009-0009-2281-7031
Drew Oldag https://orcid.org/0000-0001-6984-8411
Maxine West https://orcid.org/0009-0003-3171-3118
Colin Orion Chandler https://orcid.org/0000-0001-7335-1715

References

Acton, C., Bachman, N., Semenov, B., & Wright, E. 2018, P&SS, 150, 9
Acton, C. H. 1996, P&SS, 44, 65
Alexandersen, M., Gladman, B., Greenstreet, S., et al. 2013, Sci, 341, 994
Alexandersen, M., Gladman, B., Kavelaars, J. J., et al. 2016, AJ, 152, 111
Almeida, A. J. C., Peixinho, N., & Correia, A. C. M. 2009, A&A, 508, 1021
Annex, A., Pearson, B., Seignovert, B., et al. 2020, JOSS, 5, 2050
Astropy Collaboration, Price-Whelan, A. M., Lim, P. L., et al. 2022, ApJ, 935, 167
Astropy Collaboration, Price-Whelan, A. M., Sipőcz, B. M., et al. 2018, AJ, 156, 123
Astropy Collaboration, Robitaille, T. P., Tollerud, E. J., et al. 2013, A&A, 558, A33
Bannister, M. T., Gladman, B. J., Kavelaars, J. J., et al. 2018, ApJS, 236, 18
Beauge, C. 1994, CeMDA, 60, 225
Becker, A. C., Arraki, K., Kaib, N. A., et al. 2008, ApJL, 682, L53
Bernardinelli, P. H., Bernstein, G. M., Abbott, T. M. C., et al. 2025, AJ, 169, 305
Bernardinelli, P. H., Bernstein, G. M., Jindal, N., et al. 2023, ApJS, 269, 18
Bernardinelli, P. H., Bernstein, G. M., Sako, M., et al. 2020, ApJS, 247, 32
Bernardinelli, P. H., Bernstein, G. M., Sako, M., et al. 2022, ApJS, 258, 41
Bernstein, G. M., Trilling, D. E., Allen, R. L., et al. 2004, AJ, 128, 1364
Bianco, F. B., Ivezić, Ž., Jones, R. L., et al. 2022, ApJS, 258, 1
Bolin, B. T., Fremling, C., Morbidelli, A., et al. 2023, MNRAS, 521, L29
Bottke, W. F., Vokrouhlický, D., Marschall, R., et al. 2023, PSJ, 4, 168
Brasser, R., Mikkola, S., Huang, T. Y., Wiegert, P., & Innanen, K. 2004, MNRAS, 347, 833
Brown, M. E. 2001, AJ, 121, 2804
Brown, M. E. 2008, in The Solar System Beyond Neptune, ed. M. A. Barucci et al. (Univ. Arizona Press), 335
Buchanan, L. E., Schwamb, M. E., Fraser, W. C., et al. 2022, PSJ, 3, 9
Chen, B., Stoughton, C., Smith, J. A., et al. 2001, ApJ, 553, 184
Chen, Y.-T., Gladman, B., Volk, K., et al. 2019, AJ, 158, 214
Chen, Y.-Y., Ma, Y., & Zheng, J. 2016, MNRAS, 458, 4277
Chesley, S. R., & Veres, P. 2017, arXiv:1705.06209
Chiang, E. I., Jordan, A. B., Millis, R. L., et al. 2003, AJ, 126, 430
Chiang, E. I., & Lithwick, Y. 2005, ApJ, 628, 520
Claver, C., Bauer, A., Bechtol, K., et al. 2025, Commissioning Technical Note SITCOMTN-005, NSF-DOE Vera C. Rubin Observatory, https://sitcomtn-005.lsst.io/
Connolly, A. J., Angeli, G. Z., Chandrasekharan, S., et al. 2014, SPIE, 9150, 915014

da Costa-Luis, C., Larroque, S. K., Altendorf, K., et al. 2023, tqdm: A fast, Extensible Progress Bar for Python and CLI, v4.66.1, Zenodo, doi:10.5281/zenodo.8233425

Dalle Ore, C. M., Dalle Ore, L. V., Roush, T. L., et al. 2013, Icar, 222, 307

de Elía, G. C., Brunini, A., & di Sisto, R. P. 2008, A&A, 490, 835

de la Fuente Marcos, C., & de la Fuente Marcos, R. 2012, A&A, 547, L2

Delgado, F., & Reuter, M. A. 2016, SPIE, 9910, 991013

Delgado, F., Saha, A., Chandrasekharan, S., et al. 2014, SPIE, 9150, 915015

Dermott, S. F., & Murray, C. D. 1981, Icar, 48, 1

Dobson, M. M., Schwamb, M. E., Benecchi, S. D., et al. 2023, PSJ, 4, 75

Eggl, S., Jones, L., Jurić, M., et al. 2019, Data Management Technical Note DMTN-109, NSF-DOE Vera C. Rubin Observatory, https://dmtn-109.lsst.io/

Elliot, J. L., Kern, S. D., Clancy, K. B., et al. 2005, AJ, 129, 1117

Fedorets, G., Granvik, M., Jones, R. L., Jurić, M., & Jedicke, R. 2020, Icar, 338, 113517

Fernández, Y. R., Jewitt, D., & Ziffer, J. E. 2009, AJ, 138, 240

Fernández, Y. R., Sheppard, S. S., & Jewitt, D. C. 2003, AJ, 126, 1563

Fisher, N. I., Lewis, T., & Embleton, B. J. J. 1993, Statistical Analysis of Spherical Data (Cambridge Univ. Press)

Fraser, W. C. 2009, ApJ, 706, 119

Fraser, W. C., & Brown, M. E. 2012, ApJ, 749, 33

Fraser, W. C., Brown, M. E., Morbidelli, A., Parker, A., & Batygin, K. 2014, ApJ, 782, 100

Fraser, W. C., Pike, R. E., Marsset, M., et al. 2023, PSJ, 4, 80

Gerdes, D. W., Jennings, R. J., Bernstein, G. M., et al. 2016, AJ, 151, 39

Gilmore, G., & Reid, N. 1983, MNRAS, 202, 1025

Gladman, B., Lawler, S. M., Petit, J. M., et al. 2012, AJ, 144, 23

Gomes, R., & Nesvorný, D. 2016, A&A, 592, A146

Górski, K. M., Hivon, E., Banday, A. J., et al. 2005, ApJ, 622, 759

Grav, T., Mainzer, A. K., & Spahr, T. 2016, AJ, 151, 172

Guan, P., Zhou, L.-Y., & Li, J. 2012, RAA, 12, 1549

Gulbis, A. A. S., Elliot, J. L., Adams, E. R., et al. 2010, AJ, 140, 350

Guy, L. P., Bechtol, K., Bellm, E., et al. 2025, Rubin Technical Note RTN-011, NSF-DOE Vera C. Rubin Observatory, https://rtn-011.lsst.io/

Harris, C. R., Millman, K. J., van der Walt, S. J., et al. 2020, Natur, 585, 357

Holman, M. J., Akmal, A., Farnocchia, D., et al. 2023, PSJ, 4, 69

Holman, M. J., Bernardinelli, P. H., Schwamb, M. E., et al. 2025, AJ, 170, 97

Hoover, D. J., Seligman, D. Z., & Payne, M. J. 2022, PSJ, 3, 71

Horner, J., & Evans, N. W. 2006, MNRAS, 367, L20

Horner, J., & Lykawka, P. S. 2010, MNRAS, 402, 13

Horner, J., & Lykawka, P. S. 2012, MNRAS, 426, 159

Horner, J., Lykawka, P. S., Bannister, M. T., & Francis, P. 2012, MNRAS, 422, 2145

Hunter, J. D. 2007, CSE, 9, 90

Ivezić, Ž., Kahn, S. M., Tyson, J. A., et al. 2019, ApJ, 873, 111

Ivezić, Z. & The LSST Science Collaboration 2013, LSST Science Requirements Document Cadence Note LPM-17, http://ls.st/LPM-17

Jewitt, D. 2018, AJ, 155, 56

Jones, R. L., Chesley, S. R., Connolly, A. J., et al. 2009, EM&P, 105, 101

Jones, R. L., Slater, C. T., Moeyens, J., et al. 2018, Icar, 303, 181

Jones, R. L., Yoachim, P., Chandrasekharan, S., et al. 2014, SPIE, 9149, 91490B

Jones, R. L., Yoachim, P., Ivezic, Z., Neilsen, E. H., & Ribeiro, T. 2020, Survey Strategy and Cadence Choices for the Vera C. Rubin Observatory Legacy Survey of Space and Time (LSST), v1.2, Zenodo, doi:10.5281/zenodo.4048837

Jurić, M., Eggl, S., Moeyens, J., & Jones, R. L. 2020, Cadence Note DMTN-087, https://dmtn-087.lsst.io/

Jurić, M., Ivezić, Ž., Brooks, A., et al. 2008, ApJ, 673, 864

Kavelaars, J. J., Petit, J.-M., Gladman, B., et al. 2021, ApJL, 920, L28

Kluyver, T., Ragan-Kelley, B., Pérez, F., et al. 2016, Positioning and Power in Academic Publishing: Players, Agents and Agendas (IOS Press), 87

Kortenkamp, S. J., Malhotra, R., & Michtchenko, T. 2004, Icar, 167, 347

Kubica, J., Denneau, L., Grav, T., et al. 2007, Icar, 189, 151

Kurlander, J. A., Bernardinelli, P. H., Schwamb, M. E., et al. 2025, AJ, 170, 99

Kurlander, J. A., Holman, M. J., Bernardinelli, P. H., et al. 2025, AJ, 169, 73

Lacerda, P., Fornasier, S., Lellouch, E., et al. 2014, ApJL, 793, L2

Lam, S. K., Pitrou, A., & Seibert, S. 2015, in Proc. Second Workshop on the LLVM Compiler Infrastructure in HPC, 1

Lawler, S. M., Shankman, C., Kavelaars, J. J., et al. 2018, AJ, 155, 197

Lin, H. W., Chen, Y.-T., Holman, M. J., et al. 2016, AJ, 152, 147

Lin, H. W., Chen, Y.-T., Volk, K., et al. 2021, Icar, 361, 114391

Lin, H. W., Gerdes, D. W., Hamilton, S. J., et al. 2019, Icar, 321, 426

Lin, H.-W., Markwardt, L., Napier, K. J., Adams, F. C., & Gerdes, D. W. 2022, RNAAS, 6, 79

LSST Science Collaboration, Abell, P. A., Allison, J., et al. 2009, arXiv:0912.0201

LSST Science Collaboration, Marshall, P., Anguita, T., et al. 2017, arXiv:1708.04058

Lykawka, P. S., & Horner, J. 2010, MNRAS, 405, 1375

Lykawka, P. S., Horner, J., Jones, B. W., & Mukai, T. 2009, MNRAS, 398, 1715

Lykawka, P. S., Horner, J., Jones, B. W., & Mukai, T. 2010, MNRAS, 404, 1272

Lykawka, P. S., Horner, J., Jones, B. W., & Mukai, T. 2011, MNRAS, 412, 537

Malhotra, R. 1996, AJ, 111, 504

Malhotra, R., & Roy, S. 2023, RNAAS, 7, 143

Markwardt, L., Wen Lin, H., Gerdes, D., Adams, F. C., et al. 2023, PSJ, 4, 135

Markwardt, L., Wen Lin, H., Holler, B. J., et al. 2025, PSJ, 6, 154

Marsset, M., Fraser, W. C., Schwamb, M. E., et al. 2023, PSJ, 4, 160

Marzari, F., Tricarico, P., & Scholl, H. 2003, A&A, 410, 725

Matheson, I. C., Malhotra, R., & Keane, J. T. 2023, MNRAS, 522, 3298

McKinney, W. 2010, in Proc. 9th Python in Science Conf., ed. S. van der Walt & J. Millman (SciPy), 56

Merritt, S. R., Fedorets, G., Schwamb, M. E., et al. 2025, AJ, 170, 100

Mommert, M., Kelley, M., de Val-Borro, M., et al. 2019, JOSS, 4, 1426

Morbidelli, A., Bottke, W. F., Nesvorný, D., & Levison, H. F. 2009, Icar, 204, 558

Murray, C. D., & Dermott, S. F. 1999, Solar System Dynamics (Cambridge Univ. Press)

Murray-Clay, R. A., & Chiang, E. I. 2005, ApJ, 619, 623

Murtagh, J., Schwamb, M. E., Merritt, S. R., et al. 2025, AJ, 170, 98

Myers, J., Jones, R. L., & Axelrod, T. 2013, Cadence Note LDM-156, NSF-DOE Vera C. Rubin Observatory, https://docushare.lsst.org/docushare/dsweb/Get/LDM-156/LDM-156.pdf

Naghib, E., Yoachim, P., Vanderbei, R. J., Connolly, A. J., & Jones, R. L. 2019, AJ, 157, 151

Napier, K. J., 2020 Spacerocks, v3, GitHub, https://github.com/kjnapier/Spacerocks

Napier, K. J., & Adams, F. C. 2022, RNAAS, 6, 46

Nesvorný, D., & Morbidelli, A. 2012, AJ, 144, 117

Nesvorný, D., & Vokrouhlický, D. 2009, AJ, 137, 5003

NSF-DOE Vera C. Rubin Observatory 2025, Summary 20250930, NSF-DOE Vera C. Rubin Observatory, https://survey-strategy.lsst.io/progress/sv_status/sv_20250930.html

Olsen, K. A. G., Blum, R. D., & Rigaut, F. 2003, AJ, 126, 452

Parker, A. H. 2015, Icar, 247, 112

Parker, A. H., Buie, M. W., Osip, D. J., et al. 2013, AJ, 145, 96

Peale, S. J. 1986, in Satellites, ed. J. A. Burns & M. S. Matthews (Univ. Arizona Press), 159

Petit, J.-M., Gladman, B., Kavelaars, J. J., et al. 2023, ApJL, 947, L4

Petit, J. M., Kavelaars, J. J., Gladman, B. J., et al. 2011, AJ, 142, 131

Pike, R. E., Fraser, W. C., Volk, K., et al. 2023, PSJ, 4, 200

Pike, R. E., Kavelaars, J. J., Petit, J. M., et al. 2015, AJ, 149, 202

Pinilla-Alonso, N., Brunetto, R., De Prá, M. N., et al. 2025, NatAs, 9, 230

PyTables Developers Team 2002, PyTables: Hierarchical Datasets in Python, https://www.pytables.org/

Rein, H., Holman, M., & Akmal, A. 2023, matthewholman/assist: v1.1.1, Zenodo, doi:10.5281/zenodo.7778017

Rein, H., & Liu, S. F. 2012, A&A, 537, A128

Rein, H., & Spiegel, D. S. 2015, MNRAS, 446, 1424

Robinson, J. E., Schwamb, M. E., Jones, R. L., et al. 2025, ApJS, 279, 9

Schwamb, M. E., Fraser, W. C., Bannister, M. T., et al. 2019, ApJS, 243, 12

Schwamb, M. E., Jones, R. L., Chesley, S. R., et al. 2018, arXiv:1802.01783

Schwamb, M. E., Jones, R. L., Yoachim, P., et al. 2023, ApJS, 266, 22

SCOC 2024, Cadence Note PSTN-056, https://pstn-056.lsst.io/

Shankman, C., Gladman, B. J., Kaib, N., Kavelaars, J. J., & Petit, J. M. 2013, ApJL, 764, L2

Shankman, C., Kavelaars, J., Gladman, B. J., et al. 2016, AJ, 151, 31

Shankman, C. J. 2012, PhD thesis, University of British Columbia doi:10.14288/1.0073045

Shannon, A., Jackson, A. P., Veras, D., & Wyatt, M. 2015, MNRAS, 446, 2059

Sheppard, S. S. 2012, AJ, 144, 169

Sheppard, S. S., & Trujillo, C. A. 2006, Sci, 313, 511

Sheppard, S. S., & Trujillo, C. A. 2010a, Sci, 329, 1304

Sheppard, S. S., & Trujillo, C. A. 2010b, ApJL, 723, L233

Silsbee, K., & Tremaine, S. 2016, AJ, 152, 103

Solontoi, M., Ivezić, Ž., West, A. A., et al. 2010, Icar, 205, 605

Thébault, P., & Doressoundiram, A. 2003, Icar, 162, 27

The pandas development team 2020, pandas-dev/pandas: Pandas, v2.3.0, Zenodo, doi:10.5281/zenodo.3509134

Uieda, L., Soler, S., Rampin, R., et al. 2020, JOSS, 5, 1943

Valenti, E., Zoccali, M., Gonzalez, O. A., et al. 2016, A&A, 587, L6

van der Velden, E. 2020, JOSS, 5, 2004

Vereš, P., & Chesley, S. R. 2017, AJ, 154, 13

Virtanen, P., Gommers, R., Oliphant, T. E., et al. 2020, NatMe, 17, 261

Volk, K., Murray-Clay, R. A., Gladman, B. J., et al. 2018, AJ, 155, 260

Voyatzis, G., & Hadjidemetriou, J. D. 2005, CeMDA, 93, 263

Waskom, M. L. 2021, JOSS, 6, 3021

Wu, R.-j., Zhou, L., & Zhou, L.-y. 2019, ChA&A, 43, 262

Yoachim, P., Coughlin, M., Angeli, G. Z., et al. 2016, SPIE, 9910, 99101A

Yoachim, P., Jones, L., Eric, H., Neilsen, J., et al. 2023, lsst/rubin_sim: v2.0.0, Zenodo, doi:10.5281/zenodo.10215451

Yoachim, P., Jones, L., Eric, H., Neilsen, J., et al. 2024, lsst/rubin_scheduler: v3.4.0, Zenodo, doi:10.5281/zenodo.14232232

Zhou, L.-Y., Dvorak, R., & Sun, Y.-S. 2009, MNRAS, 398, 1217

Zhou, L.-Y., Dvorak, R., & Sun, Y.-S. 2011, MNRAS, 410, 1849

Zonca, A., Singer, L., Lenz, D., et al. 2019, JOSS, 4, 1298